Draft version March 14, 2024
Typeset using LaTeX **twocolumn** style in AASTeX62

Paβ, Hα, and Attenuation in NGC 5194 and NGC 6946

Sarah Kessler,[1] Adam Leroy,[1] Miguel Querejeta,[2] Eric Murphy,[3] David Rebolledo,[4,3] Karin Sandstrom,[5] Eva Schinnerer,[6] and Tony Wong[7]

[1] *Department of Astronomy, The Ohio State University*
4055 McPherson Laboratory, 140 West 18th Ave, Columbus, OH 43210, USA
[2] *Observatorio Astronómico Nacional (IGN), C/ Alfonso XII 3, E-28014 Madrid, Spain*
[3] *National Radio Astronomy Observatory, 520 Edgemont Road, Charlottesville, VA 22903, USA*
[4] *Joint ALMA Observatory, Alonso de Córdova 3107, Vitacura, Santiago, Chile*
[5] *Center for Astrophysics and Space Sciences, Department of Physics, University of California, San Diego*
9500 Gilman Drive, La Jolla, CA 92093, USA
[6] *Max Planck Institute for Astronomy, Kónigstuhl 17, D-69117 Heidelberg, Germany*
[7] *Department of Astronomy, University of Illinois, Urbana, IL 61801, USA*

ABSTRACT

We combine *Hubble* Space Telescope (HST) Paschen β (Paβ) imaging with ground-based, previously published Hα maps to estimate the attenuation affecting Hα, $A(H\alpha)$, across the nearby, face-on galaxies NGC 5194 and NGC 6946. We estimate $A(H\alpha)$ in $\sim$ 2,000 independent $2'' \sim 75$ pc diameter apertures in each galaxy, spanning out to a galactocentric radius of almost 10 kpc. In both galaxies, $A(H\alpha)$ drops with radius, with a bright, high attenuation inner region, though in detail the profiles differ between the two galaxies. Regions with the highest attenuation-corrected Hα luminosity show the highest attenuation, but the observed Hα luminosity of a region is not a good predictor of attenuation in our data. Consistent with much previous work, the IR-to-Hα color does a good job of predicting $A(H\alpha)$. We calculate the best-fit empirical coefficients for use combining Hα with 8, 12, 24, 70, or 100μm to correct for attenuation. These agree well with previous work but we also measure significant scatter around each of these linear relations. The local atomic plus molecular gas column density, $N(H)$, also predicts $A(H\alpha)$ well. We show that a screen with magnitude ~ 0.2 times that expected for a Milky Way gas-to-dust value does a reasonable job of explaining $A(H\alpha)$ as a function of $N(H)$. This could be expected if only $\sim 40\%$ of gas and dust directly overlap regions of Hα emission.

1. INTRODUCTION

The star formation rate (SFR) is of fundamental interest to many fields of astronomy. In order to properly understand star formation, chemical enrichment, feedback, and the evolution of star-forming galaxies, the SFR must be well measured and understood.

There are numerous methods used to derive the SFR (for reviews see Kennicutt & Evans 2012; Calzetti 2013). The most direct approach is to count the number of young stars of known age and divide by the age since formation. Unfortunately, individual stars are difficult to resolve and characterize in other galaxies. A less direct, but more widely applicable, method is to trace star formation via the highly visible signatures of young, massive stars. When present, young stars contribute most of the ultraviolet (UV) light from a galaxy. This high-energy emission is heavily absorbed by foreground dust and reprocessed into the infrared (IR). As a result, both the UV and IR are frequently employed to estimate the SFR. However, dust attenuation and sensitivity to the recent star formation history can confuse the use of the UV, while IR emission can also trace emission from older stars. As a result of these ambiguities, tracers of the number of ionizing photons, including hydrogen recombination lines and free-free emission, are often considered the least ambiguous tracer of star formation.

Ionizing photons are mostly produced by massive stars (M $>10\ M_{\odot}$) which live only for a short amount of time. The ionizations caused by these photons are balanced by recombinations. The subsequent emission of hydrogen recombination lines creates an observable tracer of the most recent (~ 10 Myr, e.g., Kennicutt 1998) star formation. Because the ionized gas is a direct result of short lived massive stars, recombinations lines are less affected by variation in the star-formation history than UV or IR emission. Disentangling ionizations due to AGN and shocks from those caused by massive stars does introduce some uncertainties, as does leakage from HII regions and emission from diffuse ionized gas (DIG). But in this paper we mainly focus on emission from bright regions in the disks of nearby star-forming galaxies, where AGN and LINER emission are not a major concern. Our aperture-based methodology will tend to minimize the contributions from DIG.

The presence of dust complicates SFR estimation based on recombination lines. Dust absorbs much of the optical recombination line emission before it reaches the

observer (again see reviews by Kennicutt & Evans 2012; Calzetti 2013). Near-infrared (NIR) recombination lines are much less effected by dust attenuation than optical lines. For example, Paβ, the NIR line that we use in this paper, suffers $\sim 3\times$ less attenuation than Hα. By combining NIR and optical recombination lines, and making assumptions about the extinction curve and dust geometry, one can calculate the amount of foreground dust present. Therefore, the combination of NIR and optical recombination lines is considered a highly reliable measure of the SFR.

In this paper, following Turner et al. (1987),Beck & Beckwith (1984),Ho et al. (1990), Scoville et al. (2003), Calzetti et al. (2005), Calzetti et al. (2007), Kennicutt et al. (2007), and Li et al. (2013), among others, we adopt this approach. We combine optical Hα and NIR Paβ recombination lines to estimate the effects of dust on recombination line emission. Hα is the $3 \rightarrow 2$ recombination line of hydrogen (at 6562.8 Å). Paβ is the $5 \rightarrow 3$ recombination line (at 1.282 μm). Assuming case B recombination with a known temperature, the ratio of Hα to Paβ in the absence of dust is known theoretically (Hummer & Storey 1987). Assuming an extinction curve (this paper uses Cardelli et al. 1989), this known ratio of Hα to Paβ allows us to accurately calculate the attenuation affecting Hα, $A(H\alpha)$.

A similar approach using the Balmer decrement, (Hα/Hβ), has been widely used (e.g., Blanc et al. 2009; Kreckel et al. 2013; Croxall et al. 2015; Catalán-Torrecilla et al. 2015; Tomičić et al. 2019, among many others). The Balmer decrement is less sensitive to dust attenuation than the Paβ-to-Hα ratio. For our adopted extinction curve and Case B recombination at $T = 10,000$ K and density 1,000 cm^{-3}, Hα is 1.3 times less attenuated by dust than Hβ (Cardelli et al. 1989). Because Paβ is emitted at a longer wavelength, for the same conditions, Paβ will be 3.2 times less attenuated by dust than Hα.

Despite their power, galaxy-wide measurements of NIR recombination lines are rare. The NIR is hard to observe from the ground due to the atmosphere, hence the popularity of the Balmer decrement. The *Hubble* Space Telescope's (HST) NICMOS instrument provided groundbreaking observations of the 4→3 recombination line of hydrogen, Paα ($\lambda = 1.875\mu$m), but the instrument was limited in its field of view (e.g., Calzetti et al. 2007; Kennicutt et al. 2007).

In this paper, we take advantage of HST's Wide Field Camera 3 (WFC3) to observe the Paβ line using narrow band imaging techniques. We present new observations of NGC 6946 and analyze archival observations of NGC 5194. Both galaxies are prime targets for recombination line observations. These are two of the nearest ($d \sim 8$ Mpc), face-on, massive actively star-forming galaxies. Both have been used to calibrate SFR estimators in the past (Calzetti et al. 2005, 2007; Kennicutt et al. 2007; Blanc et al. 2009; Murphy et al. 2011; Li et al. 2013). We combine the new Paβ images with previously published Hα to study attenuation in HII regions over the whole disk area of both galaxies.

Table 1. Adopted Galaxy Properties

Quantity	NGC 5194	NGC 6946
R.A. (J2000)	13h 29m 52.7s	20h 34m 52s
Dec. (J2000)	+47d 11h 43s	+60d 9m 11s
Dist.	8.58±0.10 Mpc	7.72± 0.32 Mpc
P.A.	173°	243°
Inclination	21°	33°
Foreground A_V	0.096 mag	0.938 mag

NOTE—Distances from McQuinn et al. (2016) for NGC 5194 and Eldridge & Xiao (2019) for NGC 6946. Orientations from Colombo et al. (2014) for NGC 5914, de Blok et al. (2008) for NGC 6946. Foreground attenuation from Schlafly & Finkbeiner (2011).

Using these measurements, we estimate $A(H\alpha)$ across these two galaxies. We place apertures across the galaxy, covering all bright Hα-emitting regions. We measure the fluxes of Paβ and Hα in each aperture and use these to calculate $A(H\alpha)$. Then, we measure the distribution of $A(H\alpha)$ and its dependence on radius. We compare $A(H\alpha)$ to the local IR-to-Hα color to test how well the local IR-to-Hα predicts $A(H\alpha)$ (following Calzetti et al. 2005, 2007; Kennicutt et al. 2007). We also compare $A(H\alpha)$ to maps of the neutral gas column density. This allows us to evaluate how well gas can be used to predict attenuation and place constraints on the relative position of the neutral gas and HII regions.

This paper is organized as follows: Section 2 describes the new and archival data used in the analysis. Section 3 explains the how we place our apertures and estimate attenuation. Section 4 describes our results.

2. DATA

2.1. *Targets*

NGC 5194 (M51) and NGC 6946 are two of the closest massive, face-on spiral galaxies. They are both gas-rich and dusty and are therefore natural targets to study the effects of attenuation on recombination line emission. Given this, both galaxies have been targets of many previous studies focused on ionizing photons. For example, NGC 5194 has targeted by Kennicutt et al. (2007), Calzetti et al. (2007), Blanc et al. (2009), and Querejeta et al. (2019). NGC 6946 has been studied by Calzetti et al. (2007), Murphy et al. (2011), Li et al. (2013), and Long et al. (2019), among others. Table 1 gives the adopted properties for each galaxy.

2.2. *HST observations*

We observed NGC 6946 (Proposal ID 14156) in Paβ with WFC3. NGC 5194 was observed in Paβ by HST as part of Proposal 12490 (P.I.: J. Koda). We retrieve these

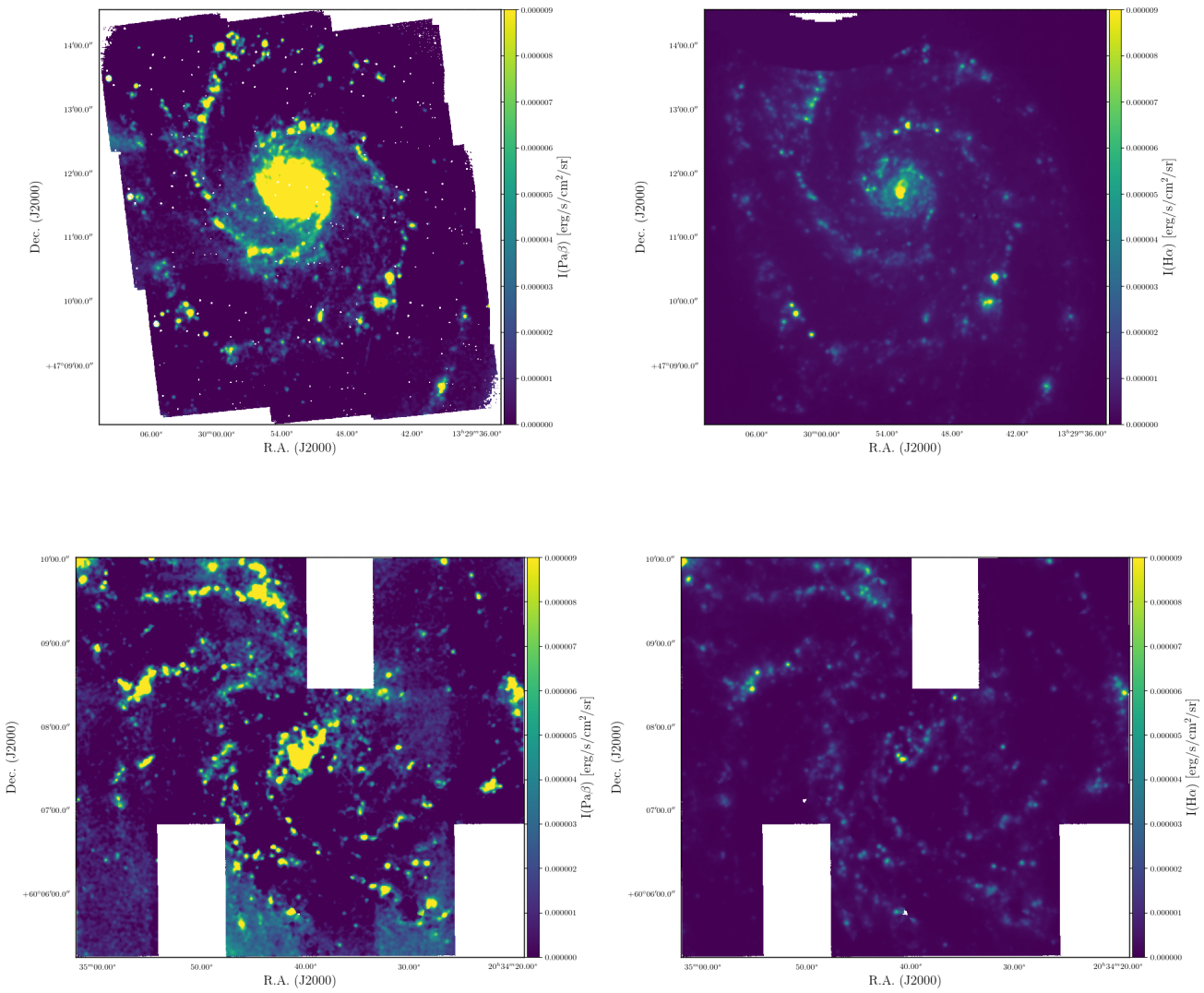

Figure 1. Images of NGC 5194 (top) and NGC 6946 (bottom) in Paβ **(left) and** Hα **(right) at our working 2″ resolution.** The images are scaled so that the intensity scales would match in the absence of attenuation. The blank regions in the NGC 6946 image reflect persistent background problems in the HST data (see Appendix).

data from the archive and analyze them in conjunction with our new observations of NGC 6946.

Both observations used WFC3's F110W and F128N filters and have a native PSF of 0.1″. F110W is WFC3's wide J filter. It has a peak wavelength of 1.150 μm and a FWHM of 0.500 μm. We use this filter to trace the stellar continuum in both galaxies. We will refer to F110W as the OFF filter. F128N is WFC3's narrow Paβ filter. It has a peak wavelength of 1.284 μm and a FWHM of 0.0128 μm. We will refer to F128N as the ON filter. The observed wavelength for Paβ changes by ≤ 0.002 μm relative to the rest value for the redshifts of NGC 5194 ($z = 0.00154 \pm 0.00001$) and NGC 6946 ($z = 0.0013 \pm 0.00001$) (Epinat et al. 2008). Therefore we expect the full line from both galaxies to lie within the F128N filter with little to no change in the transmission.

NGC 6946 was observed in nine fields which covered the area of the galaxy. NGC 5194 was observed in ten fields which covered both M51a and its companion, M51b. For our analysis we use only the nine fields associated with M51a. Using the OFF filter, each NGC 6946 field was observed for 456 seconds and each NGC 5194 field was observed for 612 seconds. In the ON filter, each NGC 6946 field was observed for 1059 seconds, and in NGC 5194 each field was observed for 2012 seconds. All observations employed a dithering pattern, and for each frame, associated sets of dithered images were combined using the WFC3 `astrodrizzle` pipeline.

The appendix steps through the details of our reduction and processing of the HST data, including background and continuum subtraction. The end result of this processing is a continuum subtracted Paβ image for each galaxy with a 2″ (FWHM) Gaussian PSF. The final Paβ line images are shown in Fig. 1.

2.3. *Archival* Hα *data*

We combine archival narrow-band Hα images with our Paβ maps to estimate the amount of dust attenuation in each region. For NGC 6946, we utilize the Hα map from Long et al. (2019). This map has already been flux calibrated and corrected for atmospheric transmission. Additionally, the filter width is small enough that significant NII contamination should not be an issue (for more details see Long et al. 2019). Based on fitting the stars in this image, we estimate the PSF to have FWHM 0.855″.

We perform the continuum subtraction ourselves. We use the narrow band OFF image described in Long et al. (2019). Because this filter does not overlap Hα, there is no risk of oversubtracting the line. Using the same methods as in Section A.3, we derive and ON-to-OFF ratio of $\beta = 0.011$ and use this to subtracting the stellar continuum. This produces an Hα line image that looks properly subtracted when visually inspected.

At our working 2″ (FWHM) resolution, the NGC 6946 map has 1σ scatter of $2.35\times\ 10^{-7}$ erg s^{-1} cm^{-2} sr^{-1}. When we place 2″ diameter apertures in apparently empty parts of the image, the rms scatter in luminosity is $8.65\times\ 10^{34}$ erg s^{-1}.

For NGC 5194 we utilize the Hα map from the *Spitzer* Infrared Nearby Galaxies Survey (SINGS; Kennicutt et al. 2003, 2007). This map has been corrected for NII contamination adopting a ratio NII/Hα = 0.6 (Kennicutt et al. 2007), which introduces an error of ∼10% or less for most regions. As a check, we verified that the SINGS map that we use matches the high quality spectral measurements from the Blanc et al. (2009) IFU map in the region of overlap.

At 2″ resolution the Hα map for NGC 5194 has 1σ scatter of $1.31\times\ 10^{-7}$ erg s^{-1} cm^{-2} sr^{-1}. When we place 2″ diameter apertures on apparently empty parts of the image, the rms scatter in the luminosity is $6.26\times\ 10^{35}$ erg s^{-1}.

2.4. *Matching point spread functions*

We convolve the Paβ and Hα maps from their native resolutions to share a Gaussian PSF with FWHM 2″. For NGC 5194 we also make a version of the maps with a FWHM of 3″. By matching the PSFs at these resolutions, we can directly compare the much higher resolution HST data to the ground-based Hα data and the VLA data. To carry out the convolution, we use astropy's (Collaboration et al. 2018) `convolve` and `Gaussian2DKernel` functions. At NGC 5194, 2″ ≈ 83 pc and 3″ ≈ 125 pc. At NGC 6946, 2″ ≈ 73 pc.

Despite our processing, the background in the Paβ maps remains unstable at a low level on large scales. This is not an issue when studying bright emission using aperture photometry at 2-3″ resolution. However, when we convolve the Paβ images to much coarser resolution, uncertainties in the background dominate the image. These appear as large-scale gradients, most likely caused by a time variable background (TVB, see Section A.1). This prevents convolution of the Paβ data to lower resolution to match the PSF of the IR images.

The backgrounds of the Hα maps appear more stable. We convolve the Hα data to 4, 7.5, 8, 9 and 11″ resolution to match that of the IR data.

2.5. *Archival infrared data*

We compare the attenuation estimated from recombination lines to archival maps of IR emission at 8 − 100μm. Both galaxies were observed by *Spitzer* at 8 and 24 μm as part of SINGS (Kennicutt et al. 2003). NGC 6946 was observed at 70 and 100μmby *Herschel* as part of KINGFISH (NGC 6946; Kennicutt et al. 2011). NGC 5194 was also observed by *Herschel* as part of the Very Nearby Galaxy Survey (VNGS, NGC 5194; Bendo et al. 2012; Mentuch Cooper et al. 2012) but only at 70μm. We also compare to 12μm data from WISE, using the maps constructed by Leroy et al. (2019).

The PSFs of these IR data are very large compared to those of the Paβ or Hα maps. Using the kernels of Aniano et al. (2011), the maps have all been convolved to have Gaussian beams with the following FWHM resolutions: 4″ (8 μm), 7.5″ (12μm), 11″ (24μm), 8″ (70 μm), and 9″ (100μm). As mentioned above, we also construct versions of the Hα map at each of these resolutions.

2.6. *Archival 33 GHz data*

We compare our recombination-line based results to the 33 GHz radio continuum map of NGC 5194 by Querejeta et al. (2019). In normal star-forming galaxies, radio emission at 33 GHz contains a large contribution from free-free emission. This free-free emission arises mostly from HII regions and is not attenuated by dust (e.g., Condon 1992; Murphy et al. 2011, 2012). As such, radio continuum emission provides a powerful alternative probe on the ionizing photon production rate. In combination with Hα, it offers an alternative way to estimate $A(H\alpha)$.

Querejeta et al. (2019) describe the observations and processing of these data. This is one of the widest area 33 GHz maps of any nearby galaxy and covers a substantial fraction of our Paβ maps. The version of the map that we use has a 3″ PSF and an rms noise of 6μJy/beam. The observations are sensitive to spatial scales up to 44″, or 1.6 kpc. Given our aperture photometry-based approach (see Sec. 3.1), we do not expect spatial filtering to represent a significant concern.

The 33 GHz map contains both free-free and synchrotron emission. For tracing ionizing photons, we

are only interested in free-free emission, and so need to correct for contamination by synchrotron emission. We adopt a thermal fraction of 70% for all apertures. This is simple, consistent with the free-free fraction found for 33 GHz peaks by Querejeta et al. (2019). We show below that this leads to good agreement with the Paβ map.

We do caution that this fixed free-free fraction might be too high for some apertures in the center of NGC 5194. There the central AGN may contribute more contaminating synchrotron emission. Linden et al. (in prep.) suggest that the thermal fraction might be ∼ 55% at 33 GHz in this region. We make no additional corrections, preferring a simple fixed 70% free-free fraction as an easy-to-reproduce check on our measurements.

2.7. *Archival gas data*

We explore how attenuation relates to the local gas column density, which we measure from 21-cm and CO emission line maps. We use 21-cm line maps from The HI Nearby Galaxy Survey (THINGS Walter et al. 2008) to trace the atomic hydrogen (HI) column density in both galaxies. We use the "natural weighted" maps, which have resolution of $11''.9 \times 10''.0$ for NGC 5194 and $6''.0 \times 5''.6$ for NGC 6946. Both resolutions are coarser than our working $2''$ resolution. We assume that the atomic gas is smooth below this resolution (e.g., see Leroy et al. 2013a). We convert these data to units of column density assuming optically thin HI and taking no account of helium. In the center of NGC 6946, **the 21-cm line** goes into absorption against the bright continuum associated with the nuclear starburst. Thus we do not derive an HI column density for the innermost point.

We use CO to estimate the column density of molecular hydrogen, H_2. For each galaxy, we use two maps, one at low resolution and one at higher resolution. The low resolution maps come from the HERACLES Survey (Leroy et al. 2009). For NGC 5194 this is a reprocessing of the data of Schuster et al. (2007). HERACLES observed the CO (2-1) line with resolution $13''.3$. High resolution CO (1-0) maps also exist for both galaxies. PAWS Schinnerer et al. (2013), observed CO (1-0) emission from the inner part of NGC 5194 at $1'' \sim 40$ pc resolution. We use a version of this map convolved to $2''.2 \sim 80$ pc resolution. Donovan Meyer et al. (2012), Rebolledo et al. (2015), and Rebolledo et al. 2020 (in prep) used CARMA to observe CO (1-0) from NGC 6946. We use a version of their map convolved to $5''.2 \sim 140$ pc resolution.

We convert from CO to H_2 column density using a standard "Galactic" conversion factor (Bolatto et al. 2013). For CO (1-0) and not including any contribution from helium this is $\alpha_{CO} = 3.2$ $M_\odot$ pc^{-2} (K km s^{-1})$^{-1}$. For the CO (2-1) maps we assume a CO (2-1)/(1-0) ratio of 0.7 (e.g., see Leroy et al. 2013b), implying $\alpha_{CO}^{2-1} = 4.6$ $M_\odot$ pc^{-2} (K km s^{-1})$^{-1}$. After converting to mass surface density, we re-express the maps equivalent column density of H_2 per cm^{-2}.

For the low resolution data we beam match the THINGS 21-cm maps to the $13.3''$ resolution of the HERACLES maps. We do not convolve the high-resolution CO maps at all, but work with them at their native resolutions. Also note that we do not apply any inclination corrections to these measurements. We compare to luminosities measured in apertures, also without inclination correction. We consider the total mean column density through the aperture to represent the relevant quantity for attenuation.

3. ANALYSIS

We focus our analysis on individual apertures. For each aperture, we subtract a local background from the Paβ and Hα maps and infer the luminosity of each line in the aperture. Using these measurements, we infer the attenuation affecting Hα in each aperture and calculate the attenuation-corrected ionizing photon production rate. We chose the aperture diameters of $2''$ and $3''$ based on the resolution of the seeing-limited Hα data ($\lesssim 2''$) and the 33 GHz VLA images ($\sim 3''$).

Our original intention was to also perform a pixel-by-pixel analysis that considers all emission. Unfortunately, the final mosaicked Paβ images show too much low level background variation to allow large scale integration or convolution to low resolution as in Li et al. (2013). In working with the individual apertures, we subtract a local background determined from the same region for both Paβ and Hα.

The zero point for the Hα appears more stable, and we can achieve robust measurements at coarser resolution. For each aperture, we also measure the IR-to-Hα color and gas column densities at a series of coarser resolutions. When we do this, we first convolve the IR, Hα, or neutral gas map. Then we measure the mean value of this low resolution map within each $2''$ or $3''$ apertures. In the limit where the new beam is large compared to the $2''$ aperture, this approaches sampling the low resolution map at the center of each aperture.

3.1. *Aperture placement*

We place apertures in each location where we would expect to detect both Paβ and Hα in the absence of dust. To set this criteria, we first measure the rms noise in the Paβ map, σ_{PB} . Then, we scale σ_{PB} ($1.46\times$ 10^{-6} erg s^{-1} cm^{-2} sr^{-1}in NGC 5194 and $5.63\times$ 10^{-7} erg s^{-1} cm^{-2} sr^{-1}in NGC 6946) to a corresponding Hα intensity assuming no dust and case B recombination, i.e., a ratio of 16.7 in NGC 5194 and 17.5 in NGC 6946.

We place apertures in regions that exceed this threshold intensity in the Hα map. That is, we place apertures everywhere that we would expect to detect Paβ at S/N> 1 based on the Hα map if there were no dust. Dust is certainly present, and any attenuation makes

the Paβ brighter compared to Hα. This makes this cut fairly conservative. To verify this, Figure 2 shows our threshold intensity contour, in yellow, on the Paβ images. This approach selects most of the bright regions in both galaxies.

In regions above the Hα threshold, we place 2″ diameter apertures. We use a square grid with adjacent apertures overlapping in area by 10%. This 2″ scale corresponds to a physical size of 73 pc at the distance of NGC 6946 and 83 pc at the distance of NGC 5194. The aperture placement is shown in Figure 2.

For NGC 5194 we repeat this exercise using 3″ diameter apertures for comparison to the 33 GHz radio continuum data of Querejeta et al. (2019) and the Hα spectroscopy of Blanc et al. (2009). NGC 6946 lacks these comparison data, and we do not make 3″ apertures for this galaxy.

By using an Hα threshold we do miss some very extinguished regions in the center of NGC 6946. These regions are absent from the Hα image, but bright in our Paβ map. If we select on Paβ instead of Hα (we make a one sigma cut in Paβ), we increase the number of apertures by $\sim 2.5\%$. As expected, the additional apertures appear in the inner, heavily extinguished part of the galaxy. In addition to these apertures appearing bright in Paβ, they also appear bright in the archival infrared continuum maps that we utilize (see Section 2).

That the apertures appear bright in both Paβ and longer wavelengths dust continuum leads us to believe that these regions are real. However, for this paper we focus only on apertures that meet our Hα threshold. In NGC 5194, we do not find any analogous cases where we would select an aperture based on Paβ but it does not appear visible in Hα emission. In this paper, we focus on studying $A(H\alpha)$, but we note that studying these heavily embedded sources in the inner part of NGC 6946 represents a good future application for our data.

In NGC 5194 we place a total of 2,075 apertures in the 2″ map and 588 apertures in the 3″ map. In NGC 6946 we place a total of 1,822 2″ diameter apertures.

3.2. *Measurements in apertures*

We subtract a local background from each aperture. We place a circular annulus around each aperture that has an inner radius of 4″ and an outer radius of 20″. We use the median value of each annuli as our local background to subtract from the corresponding aperture. For most cases these annuli are dominated by nearby empty sky instead of nearby bright emission. However, in the center of NGC 5194 these annuli are dominated by bright emission which caused us to over-subtract the background. In the center 3kpc (the deprojected galactocentric radius is calculated assuming the distance and orientation in Table 1) of NGC 5194, we used large annuli to ensure that we accurately calculated the local background. These large annuli have an inner radius of 14″ and an outer radius of 125″.

After subtracting the background, we integrate emission from each aperture to calculate the total line flux. Scaling the line flux by the distances in Table 1, we calculate L(Paβ) and L(Hα).

The 2″ diameter of the apertures matches the FWHM of the (convolved, Gaussian) PSF of both images. To account for emission associated with the part of the PSF outside the aperture, we apply an aperture correction to all measured fluxes. For a Gaussian PSF and a point source, an aperture with diameter equal the FWHM of the PSF requires an aperture correction factor of 2.0 to recover the correct flux. The aperture correction for extended sources may differ from this value. As long as Hα and Paβ show the same structure, any inaccuracy in the aperture correction will affect both lines in the same way. Therefore, we do not expect our choice of aperture correction to affect our derived extinction estimates.

These measurements, along with the inferred $A(H\alpha)$ and our best estimate uncertainties, are tabulated in Tables 2 and 3.

For each aperture, we also note: (1) The galactocentric radius, calculated assuming the distance, orientation, and inclination in Table 1. (2) The IR-to-Hα colors for IR maps at 8, 12, 24, 70, and (only for NGC 6946) 100μm. Following Section 4.2.1, these ratios are derived at lower resolution, with the exact resolution set by the IR map in question. (3) Atomic (HI), molecular (H_2), and total (HI+H_2) gas column densities at several resolutions, as described in Section 2.7. For the gas and IR-to-Hα colors, we record the mean column density or color in the aperture instead of the aperture sum. This is due to concerns about convolving our Paβ maps to match the large IR PSFs and is explained further in Section 4.2.1.

3.3. *Attenuation estimates*

Assuming Case B recombination, the ratio of Hα emission to Paβ emission in any given area should be 17.5 (at T = 10,000K and ρ = 1000 cm^{-3}) in the absence of dust (Hummer & Storey 1987). This number is relatively insensitive to the adopted density and temperature conditions. If we allow the density to range from 300 to 3,000 cm^{-3} and the temperature to range from 5,000 to 15,000 K the expected ratios range from 16.5 to 18.3.

Dust attenuates Hα emission more than Paβ emission because Hα is emitted at a shorter wavelength. In practice, this leads to a lower than expected Hα-to-Paβ ratio. Each magnitude of selective attenuation, e.g., expressed as $E(B-V)$, implies more Hα attenuation than Paβ attenuation, driving the ratio progressively lower. As a result, the difference between the expected and observed line ratio, along with an adopted extinction curve, implies some total attenuation along the line of sight.

This calculation relies on the ratios among attenuation at different wavelengths, here Hα and Paβ, remaining fixed. This is a standard assumption in the field, and

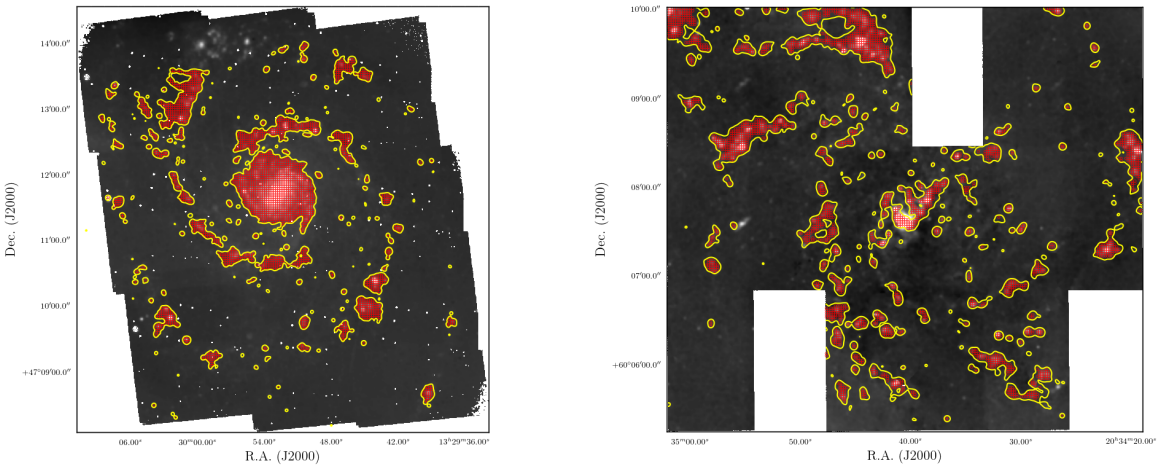

Figure 2. Paβ **images overlayed with** Hα **contours in yellow which we use to place apertures and the apertures in red.** The contours are placed where Hα is equal to the intrinsic ratio of Hα to Paβ(16.7 in NGC 5194 and 17.5 in NGC 6946) multiplied by 1 σ_{PB}. The 2″ apertures are plotted in red. This aperture placement focuses our analysis on regions of the galaxy with bright Hα. Our 1σ threshold in Hα causes us to miss a handful of heavily attenuated regions in the center of NGC 6946, but these will not substantially affect our analysis. We do not find any similar set of missed regions in NGC 5194.

Table 2. Measured Line Luminosities and Estimated Attenuation in NGC 6946

ID	R.A.	Dec.	L(Hα)	σ(L(Hα))	L(Paβ)	σ(L(Paβ))	A(Hα)	σ(A(Hα))
	(deg.)	(deg.)	(erg s^{-1})	(erg s^{-1})	(erg s^{-1})	(erg s^{-1})	(mag)	(mag)
1	308.8488	60.1622	2.1007e+37	1.5664e+36	1.8951e+36	1.0943e+36	0.7256	0.0852
2	308.8493	60.1626	2.7726e+37	1.4515e+36	2.8458e+36	1.7624e+35	0.9294	0.0583
3	308.8498	60.163	3.1386e+37	1.6424e+36	7.0358e+36	3.8189e+35	2.1635	0.0325
4	308.8504	60.1634	1.6762e+37	8.8059e+35	1.6436e+36	1.2576e+35	0.8574	0.0978
5	308.8525	60.1652	1.1600e+37	6.7633e+35	7.3008e+35	6.3087e+35	0.1569	0.7366
6	308.8535	60.166	1.6622e+38	8.7813e+36	9.9786e+36	1.6111e+36	0.0822	0.3975
7	308.854	60.1664	3.0860e+38	1.6229e+37	2.2777e+37	2.8773e+36	0.4084	0.2880
8	308.8546	60.1669	3.3841e+38	1.7715e+37	2.5994e+37	3.2914e+36	0.4716	0.2926
9	308.8474	60.162	1.3413e+37	1.2144e+36	1.2973e+36	3.4305e+35	0.8357	1.4941
10	308.8479	60.1624	3.4726e+37	2.0743e+36	3.7959e+36	5.5747e+35	1.029	0.3952
...								

Note—Luminosities and estimated attenuation for 2″ diameter apertures placed in NGC 6946. Luminosities assume the distances in Table 1. The σ quantities are our 1σ uncertainties. Details on how these uncertainties were calculated are described in Sec. 3.5 This table is a stub. We show a preview of the first 10 lines here. The full machine-readable table is available for download online.

here we assume that such an "attenuation law" holds across our target galaxies. We adopt the attenuation curve from Cardelli et al. (1989) and mostly express the total attenuation in terms of Hα. From Cardelli et al. (1989) we note the conversions 1 $mag\ A_{H\alpha} = 0.31\ mag\ A_{Pa\beta} = 0.37\ mag\ E(B-V)$.

Assuming an extinction curve, $A(H\alpha)$ is related to the ratio of Hα to Paβ via

$$\log_{10}\left(\frac{L_{H\alpha}}{L_{Pa\beta}}\right)_{obs} = \log_{10}(R_{\rm int})\cdot\frac{A(H\alpha)}{2.5}\left(\frac{k(Pa\beta)}{k(H\alpha)}-1\right) \quad (1)$$

Here $k(H\alpha)$ and $k(Pa\beta)$ correspond to the adopted reddening curves evaluated at the wavelengths of Hα and Paβ . For our fiducial adopted Cardelli et al. (1989) extinction law, $k(H\alpha) = 2.68$ and $k(Pa\beta) = 0.84$. $R_{\rm int}$ refers to the intrinsic ratio of Hα to Paβ in the absence

Table 3. Measured Line Luminosities and Estimated Attenuation in NGC 5194

ID	R.A.	Dec.	L(Hα)	σ(L(Hα))	L(Paβ)	σ(L(Paβ))	A(Hα)	σ(A(Hα))
	(deg.)	(deg.)	(erg s^{-1})	(erg s^{-1})	(erg s^{-1})	(erg s^{-1})	(mag)	(mag)
1	202.5333	47.22	2.0723e+37	1.0825e+36	1.3358e+36	1.1488e+35	0.1209	0.1381
2	202.5333	47.2205	1.9726e+37	1.0317e+36	1.9419e+36	2.1371e+35	0.7899	0.1857
3	202.5333	47.2211	1.6210e+37	8.5108e+35	1.5476e+36	2.7520e+35	0.7414	0.3206
4	202.5325	47.2116	1.5544e+37	8.1388e+35	1.7330e+36	1.4290e+35	0.9865	0.1034
5	202.5325	47.2122	1.2588e+37	6.6195e+35	1.4802e+36	1.2302e+35	1.0707	0.1215
6	202.5325	47.2127	1.4428e+37	7.5649e+35	1.4014e+36	1.3301e+35	0.7687	0.1345
7	202.5325	47.22	2.5569e+37	1.3325e+36	2.2734e+36	1.7022e+35	0.629	0.0870
8	202.5325	47.2205	2.3530e+37	1.2274e+36	3.7515e+36	3.4611e+35	1.5516	0.1124
9	202.5325	47.2211	1.2190e+37	6.4402e+35	2.4065e+36	2.2078e+35	1.8891	0.1122
10	202.5317	47.2116	1.8666e+37	9.7473e+35	1.7931e+36	2.1323e+35	0.7512	0.1550
...								

NOTE—Luminosities and estimated attenuation for 2″ diameter apertures placed in NGC 5194. Luminosities assume the distances in Table 1. The σ quantities are our 1σ uncertainties. Details on how these uncertainties were calculated are described in Sec. 3.5. This table is a stub. We show a preview of the first 10 lines here. The full machine-readable table is available for download online.

of attenuation. For NGC 5194, we adopt $R_{\rm int} = 16.7$, reflecting the temperature of T = 6300(±500)K found by Croxall et al. (2015), which reduces the expected ratio of Hα to Paβ from 17.5 (for $T = 10,000$ K) to 16.7 (Luridiana et al. 2015). For NGC 6946 we assume a temperature of $T = 10,000$ K and adopt $R_{\rm int} = 17.5$.

Rearranging Eq. 1, $A(H\alpha)$takes the form of

$$A_{H\alpha} = \frac{k(H\alpha)}{k(Pa\beta) - k(H\alpha)} \cdot 2.5 \log \frac{(H\alpha/Pa\beta)_{obs}}{(H\alpha/Pa\beta)_{int}}. \quad (2)$$

In addition to a single, fixed extinction law, Equation 2 assumes a simple geometry in which all light is processed through a foreground screen of dust. In a realistic star-forming galaxy, the geometry may be more complex. One commonly-considered more complex scenario is a "mixture model." In this scenario, dust is evenly mixed with HII regions. Some regions will experience lower total attenuation, while others experience higher total attenuation. The observed line ratio reflects the sum of light from all regions. We return to the effects of geometry in Section 4.2.4.

3.4. *Ionizing photon production rate*

Hα traces the recombination of hydrogen atoms. Photoionizations balance recombinations in HII regions. Therefore the Hα luminosity, once corrected for attenuation, directly traces the production rate of ionizing photons.

In this paper we express the rate of ionizing photon production in terms of the attenuation-corrected Hα luminosity, $L_{corr}(H\alpha)$. Because we consider individual apertures on small scales, we do not cast our results in terms of the star formation rate. But for reference and comparison to other work, we note the relationship between SFR and $L_{corr}(H\alpha)$ given in Kennicutt & Evans (2012):

$$SFR(M_\odot\ yr^{-1}) = 5.4 \times 10^{-42} L_{corr}(H\alpha)(erg\ s^{-1}). \quad (3)$$

This relation was derived by Murphy et al. (2011) using Starburst99 (Leitherer et al. 1999) model calculations for continuous star formation and a Kroupa initial mass function (Kroupa 2001) over a stellar mass range of 0.1-100M$_\odot$.

This paper focuses on the effect of attenuation on recombination line emission from HII regions, but a full accounting of ionizing photons would also require addressing direct absorption of ionizing photons by dust or leakage of ionizing photons. Both effects occur. For example see Binder & Povich (2018) for a study showing dust absorption of ionizing photons. Meanwhile there is extensive evidence showing diffuse ionized gas in our Galaxy and others. Photons leaked from HII regions represent the likely ionizing photon source for much of this diffuse ionized gas (e.g., Haffner et al. 2009).

We compare our results for NGC 5194 to the 33 GHz free-free radio continuum map of Querejeta et al. (2019). This emission traces random close encounters between protons and electrons, so that its dependence is similar to Hα, but it is largely unaffected by dust attenuation.

We utilize Equations 10 and 11 of Murphy et al. (2011) to convert between 33 GHz free-free luminosity, L_ν^T, and $L_{corr}(H\alpha)$. These equations relate the ionizing photon production rate, $Q(H^0)$, to the free-free luminosity via

$$\left[\frac{Q(H^0)}{s^{-1}}\right] = 6.3 \times 10^{25} \left(\frac{T_e}{10^4 K}\right)^{-0.45} \left(\frac{\nu}{GHz}\right)^{0.1} \times \left(\frac{L_\nu^T}{erg\ s^{-1}\ Hz^{-1}}\right), \quad (4)$$

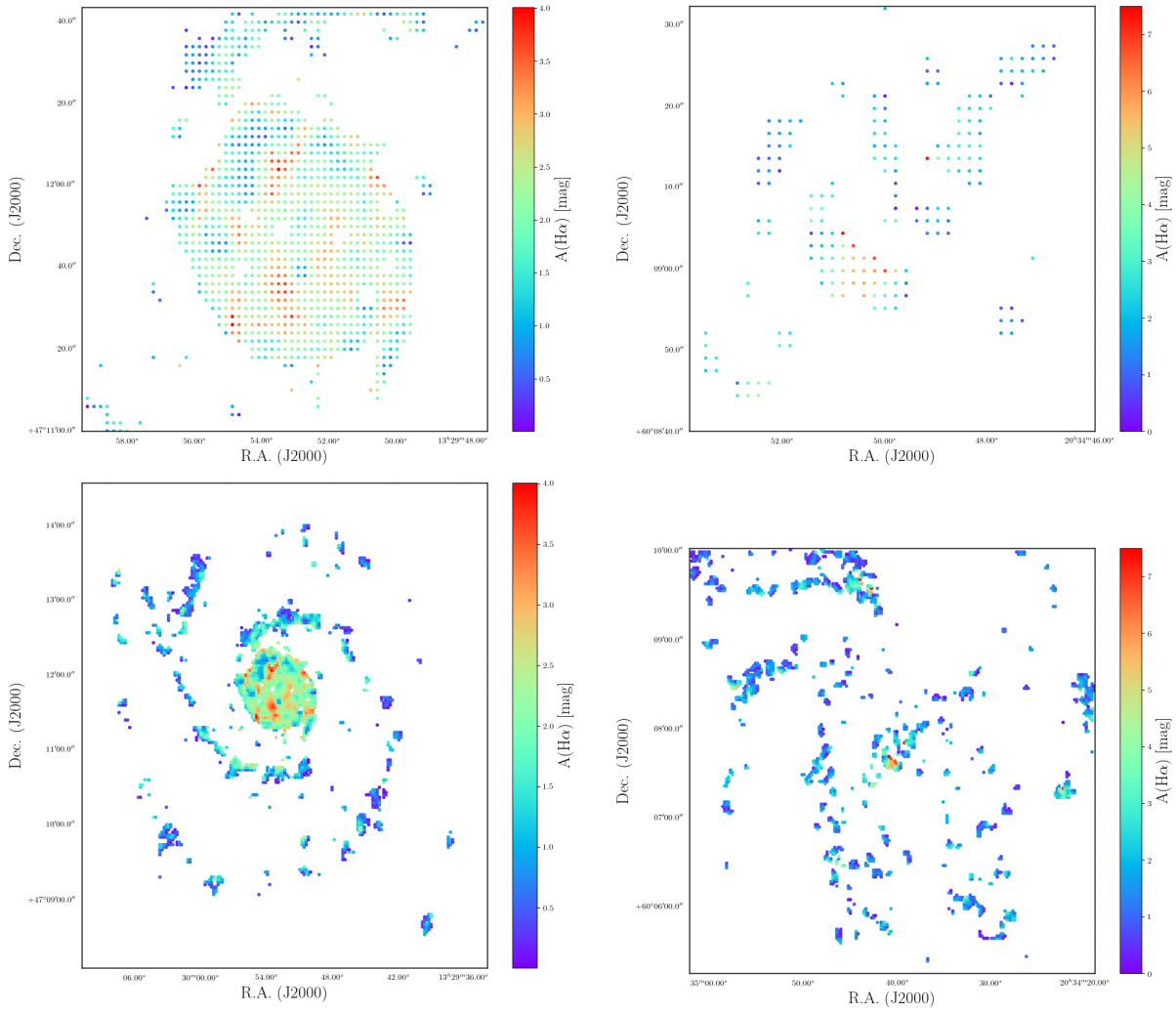

Figure 3. Spatial distribution of $A(H\alpha)$ in NGC 5194 and NGC 6946. We calculate the value of $A(H\alpha)$ in each aperture and plot the value of each aperture for NGC 5194 (left) and NGC 6946 (right). The bottom two panels cover the full galaxy. The top two panels are zoomed in to show the centers of the two galaxies.

where for us $\nu = 33$ GHz and $T_e = 6,300$ K for NGC 5194 following Croxall et al. (2015). Then, as given in Murphy et al. (2011), $Q(H^0)$ relates to the star formation rate via,

$$\left(\frac{SFR_\nu^T}{M_\odot yr^{-1}}\right) = 4.6\times10^{-28}\left(\frac{T_e}{10^4K}\right)^{-0.45}\left(\frac{\nu}{GHz}\right)^{0.1} \times\left(\frac{L_\nu^T}{erg\ s^{-1}\ Hz^{-1}}\right). \quad (5)$$

After we calculate SFR_ν^T, we use Equation 3 to convert to the equivalent $L_{corr}(H\alpha)$. We emphasize that the SFR here only represents a convenient variable to convert from $Q(H^0)$ to $L_{corr}(H\alpha)$. That is, we only use these equations together to convert 33 GHz to the predicted corresponding $L_{corr}(H\alpha)$.

3.5. *Uncertainties*

Our Paβ and Hα measurements are affected by both statistical noise and uncertainty in the background level. Our estimates of $A(H\alpha)$ also depend on the assumed extinction curve, as well as the density and temperature, which set the intrinsic Hα-to-Paβ ratio.

Statistical noise: We estimate the statistical noise in our data by placing apertures in apparently emission-free regions of each map. We placed $\sim 10,000$ apertures in each galaxy. In the appendix, we show the distribution of luminosities measured in these blank-sky apertures. As expected, the distribution appears centered on or near ~ 0 erg s^{-1}, confirming that our background subtraction appears to be working well. NGC 5194's histogram is centered slightly less than zero at -7.52×10^{-34} $erg\ s^{-1}$ but this is controlled for in our analysis by local background subtraction. We adopt the rms scatter in the luminosity measured for these appar-

ently empty apertures as our estimate of the statistical noise.

For NGC 5194 we estimate statistical noise of $\sigma_{Pa\beta} = 6.3 \times 10^{35}$ erg s^{-1} for Paβ and $\sigma_{H\alpha} = 6.8 \times 10^{35}$ erg s^{-1} for Hα. For NGC 6946 we estimate statistical noise of $\sigma_{Pa\beta} = 8.7 \times 10^{34}$ erg s^{-1} for Paβ and $\sigma_{H\alpha} = 9.1 \times 10^{34}$ erg s^{-1} for Hα.

Zero point uncertainty: We used an empirical approach to continuum subtraction, bootstrapping the appropriate ratio to translate OFF emission to a continuum estimate from the data themselves. This process has some associated uncertainty. We estimate the magnitude of this uncertainty by making six maps that range from being visibly slightly over-subtracted to slightly under-subtracted.

We allow our Monte Carlo error estimation (described below) to randomly choose between one of these maps. This allows us to quantify the error associated with our continuum subtraction. Based on this exercise, we estimate the rms uncertainty in the overall background level to be 7.00$\times$ 10^{36} erg s^{-1} in Paβ and 3.00$\times$ 10^{37} erg s^{-1} in Hα for NGC 5194. In NGC 6946 we estimate the degree of rms uncertainty in the overall background level to be 1.11$\times$ 10^{36} erg s^{-1} in Paβ and 2.12$\times$ 10^{37} erg s^{-1} in Hα.

Note that unlike the statistical noise, this uncertain background will affect all (or at least many) apertures in tandem.

Combined uncertainty estimates: We estimate the total uncertainty on each measured luminosity and calculated $A(H\alpha)$ value by running a Monte Carlo simulation.

We treat our measurements as the "true" values. Then we add statistical noise, apply other sources of uncertainty, and repeat our calculations. We aim to allow any variables that might affect the final value of $A(H\alpha)$ to vary across a realistic range.

Specifically, we do the following, beginning with our true measurements:

1. Add normally distributed statistical noise to each L(Hα) and L(Paβ) value with the magnitude noted above.

2. Perturb the zero point of all L(Hα) and L(Paβ) by adding or subtracting the photometric calibration error. This error can vary between $5-7\%$ and we therefore we choose a random error of either 5%, 6%, and 7%.

3. Choose randomly from six Paβ maps where the continuum is visibly over and under subtracted to various degrees.

4. Allow the temperature and density used to calculate the intrinsic line ratio to vary. For the temperature, we choose a random temperature from a Gaussian distribution with FWHM 1,000 K centered on the median temperature of the galaxy [6,300 K for NGC 5194 Querejeta et al. (2019) and 10,000 K for NGC 6946 Murphy et al. (2011)]. For the density, we any allow density between 100-10,000 cm^{-3} in linear space.

5. Randomly choose between the Cardelli et al. (1989) extinction curve and the Fitzpatrick (1999) extinction curve.

We ran 1,000 simulations. We adopt the rms scatter in the measured luminosities and $A(H\alpha)$ as our best-estimate uncertainty. For $A(H\alpha)$, we find rms scatter of 0.35 mag in NGC 5194 and 0.20 mag in NGC 6946. In Tables 3 and 2 we use this calculation to report 1σ values for each reported quantity.

3.6. *Comparison to literature measurements*

There has not been previous wide-field Paβ imaging of either of our targets, but both NGC 5194 and NGC 6946 have multiple previous estimates of $A(H\alpha)$. NGC 5194, in particular, has been a key target for calibrating recipes to correct Hα for the effects of attenuation.

3.6.1. *NGC 5194*

Large area 33 GHz map: The recent 33 GHz radio continuum map by Querejeta et al. (2019) covers a large part of NGC 5194. We measure 33 GHz luminosities in matched apertures from the 33 GHz map and our own data, following the same local background subtraction method detailed in 3.1. In this paper we assume that the free-free makes up 70% of the total 33 GHz radio emission across all apertures. This might overestimate the free-free emission in the central 3 kpc which might be affected by NGC 5194's central AGN (see Section 2). Then, we re-express the free-free luminosity as attenuation-corrected Hα following Section 3.4.

In Figure 4 we compare results from the Querejeta et al. (2019) free-free map to the corrected Hα from our Paβ based measurements. We compare the extinction-corrected Hα luminosities from the two methods in the left panel and $A(H\alpha)$ in the right panel. We obtain an effective attenuation for the 33 GHz data by comparing it to our Hα image and assuming the 33 GHz data is not attenuated by dust.

Overall the two approaches to estimate $A(H\alpha)$ agree fairly well. Considering the corrected Hα luminosity, the value estimated from free-free emission is median 0.88 times that estimated from Paβ and Hα, with rms scatter in the ratio of 0.07 dex. If the free-free fraction were allowed to shift to ~ 0.8, the two data sets would show a median ratio of ~ 1.

Figure 4 also shows $A(H\alpha)$ as a function of galactocentric radius, plotting results for both the free-free and Paβ-based approaches. The figure shows that in the central 2 kpc the $A(H\alpha)$ from our Paβ approach is higher than that from the free-free approach. At

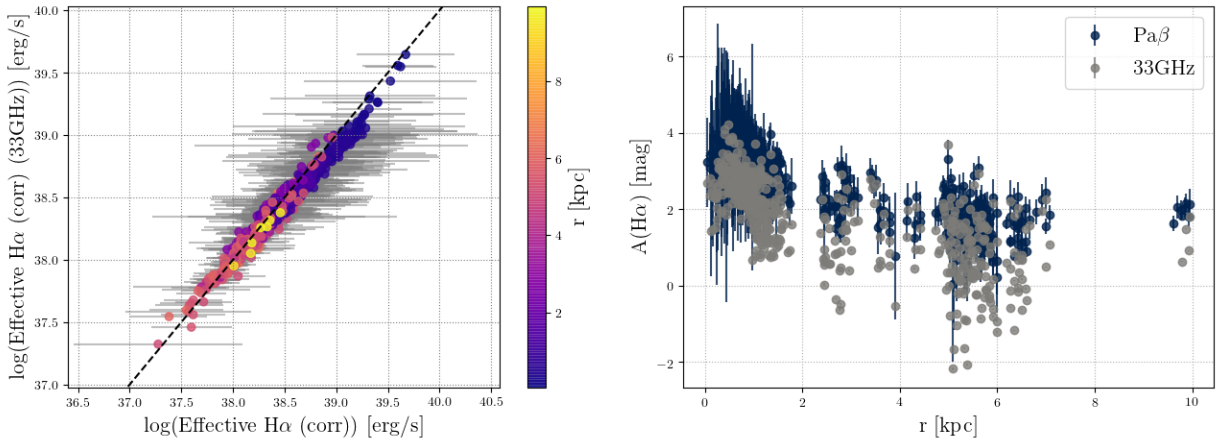

Figure 4. Comparison of our measurements to 33 GHz radio continuum. Left: Extinction-corrected Hα luminosity estimated from 33 GHz free-free radio continuum emission (Querejeta et al. 2019) as a function of our attenuation-corrected Hα emission estimates from combining Paβ and Hα. When estimating the extinction corrected Hα luminosity, we assume that 70% of the 33 GHz emission comes from free-free emission. Each point corresponds to measurements for a 3″ aperture in NGC 5194, with apertures color-coded by radius. The dashed line shows the one-to-one line expected for perfect agreement. Across all apertures, the median ratio of 33 GHz-based Hα luminosity to our estimate corrected Hα luminosity is 0.88 with 0.07 dex rms scatter. This shows good overall agreement between these t. **Right**: Two estimates of Hα attenuation, $A(H\alpha)$, as a function of galactocentric radius. In black, we show $A(H\alpha)$ estimated by comparing Paβ and Hα. In gray, we show $A(H\alpha)$ estimated by comparing Hα to 33 GHz emission. As shown in the panel on the left, the Paβ-to-Hα approach shows overall good agreement but yields slightly higher attenuation than the Hα to radio continuum. The biggest differences come in the inner part of the galaxy.

larger radii, the free-free emission predicts slightly larger $A(H\alpha)$ than the Paβ. Again in terms of corrected Hα luminosity, the median ratio (free-free-based estimate to Paβ-based-estimate) inside 2 kpc is 0.63 with a rms scatter in the ratio 0.99 mag. The median ratio in the outer 3-9 kpc is 1.32 with a rms scatter in the ratio of 0.19 mag.

We expect the two approaches to yield the same result, so this comparison suggests a $\sim \pm 30\%$ uncertainty on the final attenuation-corrected luminosities. Some of these differences might result from flux calibration uncertainties and uncertainties in background subtraction. The fraction of the radio emission arising from free-free emission also represents an uncertainty. We adopted a constant free-free fraction (see Section 2), but this quantity likely might vary spatially (e.g., see discussion in Querejeta et al. 2019), which might create some of the gradient.

In the very center of the galaxy, NGC 5194's AGN likely plays a role. The likely impact of the AGN will be to contribute additional synchrotron emission. In this case the fraction of the radio coming from free-free emission will be smaller at the center of the galaxy than in the surrounding regions. There is some evidence for this already in Figure 4. In the left panel, the highest luminosity points correspond to the center. These curve up towards equality, showing higher 33 GHz emission relative to the surrounding (blue and purple) points. Querejeta et al. (2019) estimated the thermal fraction from the spectral index and found that it is smaller in the center. In fact the area where the thermal fraction is smaller precisely coincides with the area of the AGN radio plasma jet as seen at other radio wavelengths. This is nicely confirmed in Fig. 4.

Recombination line measurements from the inner 2 kpc: The inner part of NGC 5194 has been observed in recombination line emission and radio free-free emission many times, with attenuation estimated in studies by Calzetti et al. (2005), Kennicutt et al. (2007), Calzetti et al. (2007), Blanc et al. (2009), and Querejeta et al. (2019) among others.

We compare our Paβ-based attenuation measurements to attenuation estimates based on Paα measurements from Kennicutt et al. (2007), Balmer decrement measurements from Blanc et al. (2009), and 33 GHz measurements from Querejeta et al. (2019) in Fig. 5.

For this exercise we use the aperture locations and size (4.3″in diameter) specified in Blanc et al. (2009) to remeasure our Paβ maps and the 33 GHz maps. The aperture locations in Blanc et al. (2009) cover the inner $4.1 \times 4.1 kpc^2$ of NGC 5194. Here we limit the analysis to only the apertures that also meet the Hα intensity threshold described in Section 3.

We use local background subtraction as in Section 3 to correct for any background variances in the Hα, Paβ, and 33 GHz emission images. We find that our results can be very sensitive to the background definition in the center on NGC 5194 due to its large size. To ensure we

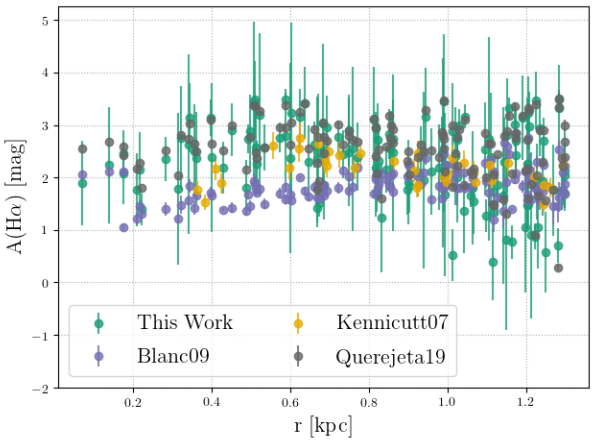

Figure 5. Comparisons to past literature in NGC 5194. Plotted are $A(H\alpha)$ measurements at aperture locations and sizes from Blanc et al. (2009). Our measurements agree well with both Kennicutt et al. (2007) and attenuation measurements derived using the 33 GHz map from Querejeta et al. (2019) and Hα assuming the 33 GHz emission is not affected by attenuation. The Balmer decrements measurements by Blanc et al. (2009) provided lower values of $A(H\alpha)$ in the very center of the galaxy. This might reflect to the breakdown of the Balmer decrement at high values of $A(H\alpha)$ or issues with our aperture photometry in such a crowded, bright region.

do not over-subtract the center apertures we use local annuli large enough to sample the empty space around the galaxy center. However, this might bias us to lower background values, and thus we could predict larger luminosities in the galaxy center than is true.

Outside the central 0.3 kpc, our measurements agree well with both the 33 GHz data and the Paα measurements from Kennicutt et al. (2007) at values of $r > 0.4kpc$. Where $r < 0.4kpc$, we estimate higher values of $A(H\alpha)$. The disagreement of Paβ corrected Hα and 33 GHz in the galaxy center of NGC 5194 might be caused by our adopted radial gradient converting the 33 GHz data to free free-free emission discussed in Sec. 3.6

The Balmer decrement measurements from Blanc et al. (2009) are lower than other measurements in the inner ∼0.6 kpc of the galaxy. This might imply a mild deviation from a screen geometry, with the Balmer emission being absorbed more easily by higher values of $A(H\alpha)$.

3.6.2. *NGC 6946*

Recombination line measurements of NGC 6946 are not as plentiful as NGC 5194, perhaps due to its low Galactic latitude.

Wide field Brγ imaging: Li et al. (2013) mapped NGC 6946 in $Br\gamma$ using the WIRCam (Wide Infrared Camera) on CFHT (CanadaFranceHawaii Telescope). This $Br\gamma$ map was used with the SINGS Hα map to obtain attenuation-corrected Hα values, and thus a SFR.

Their reported median value of $E(B-V)$ is 0.44 mag. This corresponds to A_V of 1.36 mag assuming $R_V = 3.1$ and a Cardelli et al. (1989). Our result is slightly higher at $A_V = 1.76$ mag $\pm$ 0.20 mag.

Part of this discrepancy can be explained by aperture placement. The very center of NGC 6946, where we see our highest values of attenuation, is excluded from the Li et al. (2013) analysis. Additionally, our apertures are 2″ in diameter. Li et al. (2013) use 12″ diameter apertures. The larger apertures used by Li et al. (2013) might mix low attenuation and high attenuation regions, leading to a lower median attenuation. We also use a different Hα map (we use the one from Long et al. 2019, while they use the SINGS map).

Low resolution free-free emission: (Murphy et al. 2011) measured the 33 GHz emission in the nucleus and 9 extra-nuclear regions across NGC 6946. These regions were measured in apertures that were 25″ in diameter. They generally found good agreement between the SFR diagnostics and 33 GHz emission. However, in the center the dust-inferred SFR was a factor of 2 larger than that derived using radio data. This was attributed to an accumulation of non-ionizing stars in the center of the galaxy due to an extended episode of star formation.

Attenuation in the nucleus: We can also compare our median measured attenuation in Hα for the nuclear region (which we roughly define here as the central kiloparsec), 2.54 mag, to previous estimates. The attenuation in the nucleus of NGC 6946 has previously been reported as $A_V = 4.3$ mag (aperture size of 280pc, based on the Balmer decrement Engelbracht et al. 1996), $A_V =$ 4.7 mag(90pc aperture size, Balmer decrement Quillen & Yukita 2001), and $A_V = 5.0$ mag (1 kpc, 9.7μm silicate absorption feature Smith et al. 2007). Values of A_V have been recorded even higher with attenuation robust IR and Radio data. Tsai et al. (2013) measured $A_V \sim 25$ ($A(H\alpha)$∼22) for the central 200 pc using Brγ data. Using radio-based gas mass estimates, Schinnerer et al. (2006) estimated the total attenuation in the central ∼60pc and found much higher attenuation, as large as $A_V \sim 100$ mag.

In order to compare our results, we convert our measured values of $A(H\alpha)$ to A_V using a Cardelli et al. (1989) extinction curve with $R_v = 3.1$. We only have 1 aperture which covers the central 60pc as our aperture size in NGC 6946 is 73 pc. This aperture has a measured $A(H\alpha)$ of 4.0 mag ($A_V = 4.63$ mag). Engelbracht et al. (1996), Quillen & Yukita (2001), and Smith et al. (2007) found median A_V attenuation within the central kpc, 280pc, and 90pc to be 2.93 mag, 4.77 mag, and 4.36 mag with a scatter of 1.88 mag, 2.09 mag, and 0.67 mag. Given the differences in aperture definitions and methods, there appears to be good overall agreement between their measurements and ours. We take this as

a qualitative confirmation of our measurement, at least at the factor of ~ 2 level.

The much larger values of $A_V \sim 100$ mag from Schinnerer et al. (2006) likely mainly reflect methodological differences. While our measurements and the Balmer decrement measurements reflect observed recombination line emission, the Schinnerer et al. (2006) estimate expresses the extinction expected based on all of the gas present. The HII regions and gas might not be coincident or the HII regions and gas might be mixed, with some of the HII regions so heavily embedded as to be practically invisible. In either case, geometry can go a long way towards explaining the discrepancy. We return to a similar point comparing emission-based column densities to our absorption measurements in Section 4.2.4.

4. RESULTS

We constructed Paβ line emission maps of NGC 5194 and NGC 6946 (Section A.4). Images of these maps appear in Figure 1.

We compared these Paβ maps to Hα maps from Kennicutt et al. (2007) and Long et al. (2019) to calculate the implied Hα attenuation and the attenuation-corrected Hα luminosity in 2,075 apertures in NGC 5194 and 1,934 apertures in NGC 6946 (Section 3). These measurements are tabulated in Tables 2 and 3.

Our maps have wide area, so that the apertures span a large range of galactocentric radius, IR-to-Hα color, and gas column density. Note, however, that uncertainties in the background level of the Paβ maps restrict our analysis to regions that are relatively bright in both Paβ and Hα. Our apertures include 50% of the total Hα emission (uncorrected for attenuation) from NGC 5194 and 49% of the total Hα emission from NGC 6946. Although not ideal, this focus on bright regions while subtracting a surrounding "diffuse" component follows previous work in the field.

We use these measurements to infer the distribution and radial profile of $A(H\alpha)$ in each galaxy (Section 4.1). We then test several methods of predicting $A(H\alpha)$ based on location in the galaxy or measurements at other wavelengths (Section 4.2).

4.1. *Distribution of $A(H\alpha)$*

Figure 6 shows the distribution of $A(H\alpha)$ in each galaxy. The left panel plots the histogram treating each aperture equally. The right shows the distribution of attenuation-corrected L(Hα) as a function of $A(H\alpha)$. Table 6 quantifies both distributions.

Treating all apertures equally, the distribution of $A(H\alpha)$ appears similar between the two galaxies. Both galaxies show a median $A(H\alpha)$ near $\sim$ 1.5 mag, with 67% of the data lying within roughly ±1 mag of this median value. These values may be biased somewhat high by our selection of bright apertures, but as we saw above that they agree well with past results. This distribution also appears consistent with measurements by Murphy et al. (2018). They found a median $A(H\alpha)$ value of 1.26 ± 0.09 mag with scatter of 0.87 mag for 162 pointings towards star forming regions across 56 nearby galaxies (with measurements on 30-300 pc scales).

Table 4. Distribution of $A(H\alpha)$.

Quantity	NGC 5194	NGC 6946
By number[a]		
... 16th percentile	0.55 mag	0.72 mag
... median (50th percentile)	1.41 mag	1.52 mag
... 84th percentile	2.39 mag	2.49 mag
By luminosity[b]		
... 16th percentile	1.15 mag	1.62 mag
... median (50th percentile)	2.19 mag	3.37 mag
... 84th percentile	2.86 mag	5.67 mag

[a] Distribution of $A(H\alpha)$ treating each aperture as an equal, independent measurement.

[b] Distribution of $A(H\alpha)$ sorted by the attenuation-corrected Hα luminosity associated with each aperture.

Note—Distributions considering measurements from our apertures, which capture $\sim$ 50% of the Hα emission from each target.

The histogram of attenuation-corrected Hα luminosity shifts to higher values compared to the histogram treating all apertures equally. That is, the more intrinsically luminous HII regions also tend to be more heavily embedded, with much of the Hα emission from a galaxy occurring in regions of high $A(H\alpha)$. We return to this point below.

Both sets of histograms show structure (e.g., tails and multiple peaks) that corresponds to the morphology of the galaxies. This appears particularly prevalent in the luminosity-weighted histogram. Much of this variation in $A(H\alpha)$ occurs as a function of radius. We plot this directly, showing $A(H\alpha)$ as a function of galactocentric radius in Figure 7.

We observe an overall radial trend in both galaxies. On average, central regions show higher $A(H\alpha)$ than regions at large radius. NGC 5194 has a large and bright central region, which causes more than 15% of the apertures to be placed in the center of the galaxy.

This radial trend leads to a bimodal distribution in both histograms in Figure 6. The inner part of the galaxy shows significantly higher attenuation compared to the outer regions. As a result, the two regions appear somewhat distinct in the distributions. The median value of $A(H\alpha)$ for apertures with galactocentric radius less then 1 kpc is 2.36 mag. By contrast, the median $A(H\alpha)$ of apertures with galactocentric radius greater than 1 kpc is 1.14 mag.

The large range of attenuation for NGC 6946 also mostly reflects high attenuation in the galaxy center. The center of NGC 6946 hosts a concentration of molec-

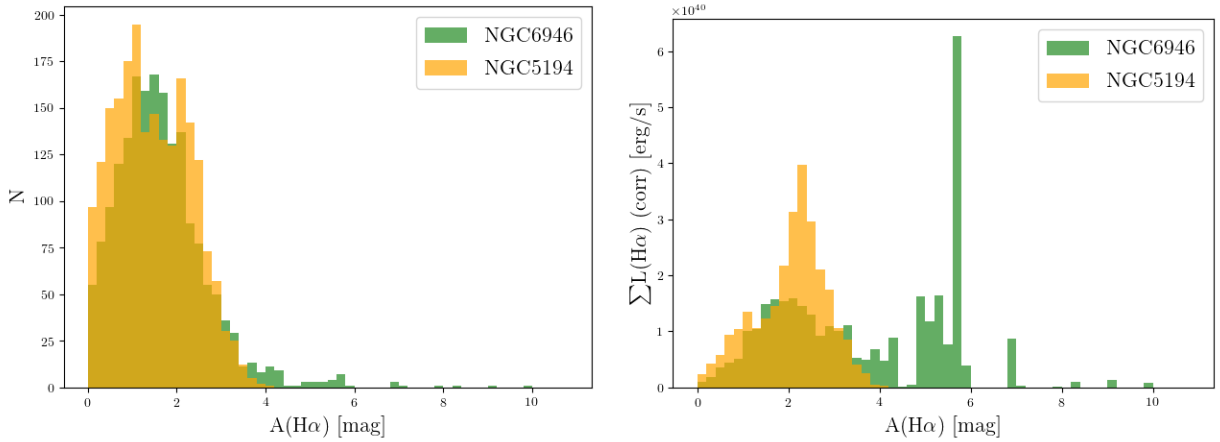

Figure 6. Distribution of $A(H\alpha)$ in apertures across NGC 5194 and NGC 6946 Left: Histogram of the distribution of $A(H\alpha)$ across NGC 5194 (orange) and NGC 6946 (green), treating each aperture equally. Right: Total attenuation-corrected Hα luminosity contributed by apertures in each bin of $A(H\alpha)$. In both panels, the bins have width of 0.2 mag in $A(H\alpha)$.

ular gas funneled to the center by an inner stellar bar (Schinnerer et al. 2006). This leads to high gas column densities and correspondingly high attenuations. This gas also forms stars, so that the center of NGC 6946 represents a prime example of a bar-fed nuclear starburst (e.g., see Murphy et al. 2011).

The very center of NGC 6946 appears more extreme than that of NGC 5194, but the gas also appears more concentrated. While the peak attenuations reach $\gtrsim$ 4 mag in the center, they approach the disk-averaged values by $\sim$ 1 kpc. By contrast, NGC 5194 shows a more gradual decline in attenuation, with high values out to $\sim$ 2 kpc.

Even our high estimates for the central attenuation may underestimate the true values in the innermost part of NGC 6946. The center hardly appears visible in Hα and UV light, so that half of the galaxy center visible in the Paβ image is not visible in the Hα image (see Figure 2). This might suggest that much of the center might have even higher attenuations than we calculate in our analysis. In fact, Tsai et al. (2013) measured $A_V \sim 25$ ($A(H\alpha)\sim$22) for the central 200 pc using Brγ data. Brγ at 2.17μm, is even more dust robust than Paβimplying that some of our Paβ emission is likely attenuated before we can observe it.

A few extranuclear regions in NGC 6946 also show very high attenuation. These are visible in both the maps (Fig. 3) and radial profiles (Figure 7). While these regions show high $A(H\alpha)$, they have only relatively weak actual Hα luminosity. On average, their Hα intensity is only 10% of the median value of L(Hα) for all apertures in the galaxy. More, these high $A(H\alpha)$, low Hα regions tend to lie near the edge of brighter regions. It is possible that these regions represent a handful of deeply enshrouded, young regions. But given their location and faintness, we suspect that these high $A(H\alpha)$ mostly reflect instability in the image processing (e.g., local problems with the background subtraction, reprojection, and convolution of the images). Overall, only a few such regions appear in our data, and none are obvious in NGC 5194, so the effect is likely fairly limited.

While these radial gradients give a good first-order picture, both galaxies show significant scatter in $A(H\alpha)$ at fixed galactocentric radius. In NGC 5194 the typical rms scatter in $A(H\alpha)$ within a 1 kpc bin is $\approx$ 0.55 mag. NGC 6946 shows even a higher variation, with rms scatter of $\approx$ 1.0 mag per 1 kpc bin. In the next sections, we look at how $A(H\alpha)$ correlates with other quantities.

4.2. *Relation between $A(H\alpha)$ and other observable quantities*

Mapping Paschen β across two of the brightest, nearest star-forming galaxies required a significant time investment from *Hubble*. Given the difficulty in obtaining these "gold standard" estimates of the ionizing photon rate, it has become standard practice to predict $A(H\alpha)$ via other less direct means (see Section 1). A main motivation for obtaining and analyzing these maps was to further evaluate common empirical prescriptions for $A(H\alpha)$.

In this section, we compare our $A(H\alpha)$ estimates to the local Hα-to-infrared color, the Hα luminosity of the region, galactocentric radius, and the local gas column density. We evaluate the ability of each quantity to predict $A(H\alpha)$ in one or both galaxies. We measure the scatter, and calibrate free parameters in the empirical prescriptions. We tabulate these results in table 5.

4.2.1. *$A(H\alpha)$ from Hα and infrared emission*

Calzetti et al. (2007) and Kennicutt et al. (2007) showed that $A(H\alpha)$ can be estimated from the ratio of infrared to Hα emission. Where there is more IR emission relative to Hα, the Hα line tends to suffer from more attenuation. Because IR measurements have become plentiful thanks to *Spitzer*, *Herschel*, and WISE,

Table 5. Scatter around predictive models

	$H\alpha + \alpha \cdot 8\mu m$	$H\alpha + \alpha \cdot 12\mu m$	$H\alpha + \alpha \cdot 24\mu m$	$H\alpha + \alpha \cdot 70\mu m$	$H\alpha + \alpha \cdot 100\mu m$	Gas (β·Screen)	Gas (Mixture)	r
	NGC 5194							
Linear (mag.)	0.330	0.339	0.338	0.327	–	0.702	0.109	0.318
Log (dex)	0.044	0.045	0.046	0.044	–	0.099	0.218	0.105
	NGC 6946							
Linear (mag.)	0.200	0.272	0.252	0.200	0.213	0.255	0.248	0.251
Log (dex)	0.121	0.105	0.109	0.121	0.118	0.363	0.078	0.054
	Both Galaxies							
Linear (mag.)	0.149	0.178	0.160	0.135	–	0.352	0.112	0.157
Log (dex)	0.085	0.082	0.084	0.088	–	0.338	0.116	0.0944

Note—**Scatter in our data about empirical models to predicts** $A(H\alpha)$. The values of α used in the first four columns can be found in table 6. We use our best-fit value for α for all wavelengths. For comparison, the scatter in the data alone, without any model prediction, is 0.84 mag (0.38 dex) in NGC 5194 and 1.04 mag (0.36 dex) in NGC 6946.

Table 6. Correlation coefficients and best fit predictions of $A(H\alpha)$ and IR bands

Quantity	NGC 5194	NGC 6946	Both Galaxies
	8μm		
Res. 8μm	4″	4″	4″
r(8μm)	-0.46	-0.58	-0.03
α(8μm)	0.009± 0.003	0.014 ± 0.004	0.014 ± 0.004
α(8μm) Kenn. 09		0.011±0.003	
	12μm		
Res. 12μm	7.5″	7.5″	7.5″
r(12μm)	-0.56	-0.51	-0.04
α(12μm)	0.025± 0.015	0.089± 0.027	0.051± 0.015
	24μm		
Res. 24μm	11″	11″	11″
r(24μm)	-0.48	-0.53	-0.05
α(24μm)	0.029± 0.009	0.049± 0.015	0.047± 0.010
α(24μm) Kenn. 07		0.038±0.005	
α(24μm) Calz. 07		0.031± 0.006	
	70μm		
Res. 70μm	8″	8″	8″
r(70μm)	-0.59	-0.55	-0.04
α(70μm)	0.008± 0.003	0.014 ± 0.004	0.013± 0.004
α(70μm) Li 13		0.011±0.001	
	100μm		
Res. 100μm	–	9″	–
r(100μm)	–	-0.52	–
α(100μm)	–	0.018± 0.005	–

Note—We tabulate the image resolution, rank correlation coefficients (r), and best fit linear coefficient
used to create a linear model.

this comparison to IR emission now represents a main way to estimate $A(H\alpha)$.

As discussed in Section 2, we do not consider the background level of our Paβ maps stable enough to measure a robust intensity at the low resolution of our IR data (4, 7.5, 11, 8, and 9″ for the 8, 12, 24, 70, and 100μm bands respectively). There is simply too much uncertain, low-level background structure involved in the convolution to yield a robust result.

To work around this limitation, we compare $A(H\alpha)$ estimated from combining Paβ and Hα within our 2″ apertures to the Hα-to-IR ratio measured at lower resolution. We convolve the archival Hα images to match the PSF of each IR band. We then divide the Hα image by the IR bands to create an Hα-to-IR ratio image for each IR band at the lower IR resolution. We sample these lower resolution images using the same aperture locations and sizes used to create our high resolution attenuation maps (see Section 3).

This approach yields low resolution Hα-to-IR colors, which we compare to high resolution attenuation estimates. This situation actually resembles a common application of these prescriptions. The PSF of IR telescopes is almost always poor compared to that of seeing-limited optical images. The case that we consider resembles using low-resolution IR data to attempt to correct a high-resolution Hα map for attenuation.

Before sampling we verify that the median values of apertures placed on empty sky was indeed 0 erg s^{-1} cm^{-2} (or not a number if the IR band in the denominator had a ~ 0 background). We do not conduct local background subtraction on any measurements used to calculate the Hα-to-IR ratio. Instead we simply take the sum of the aperture and divide that by the aperture area to obtain an average IR value. This might bias us somewhat high in IR, which would bias our Hα-to-IR value low. We tested this by applying apertures the size of the PSF to the image. We compared the results we have with a PSF sized aperture to those calculated with our adopted 2″ aperture. The median difference between the Hα-to-IR ratio to the Hα-to-IR ratio was 0.15 mag with a scatter of 0.09 mag. This indicates that we may be underestimating our Hα-to-IR ratio, but only slightly.

We compare this lower-resolution Hα-to-infrared ratio to our Paβ-based $A(H\alpha)$ estimates in Figures 8 and 9.

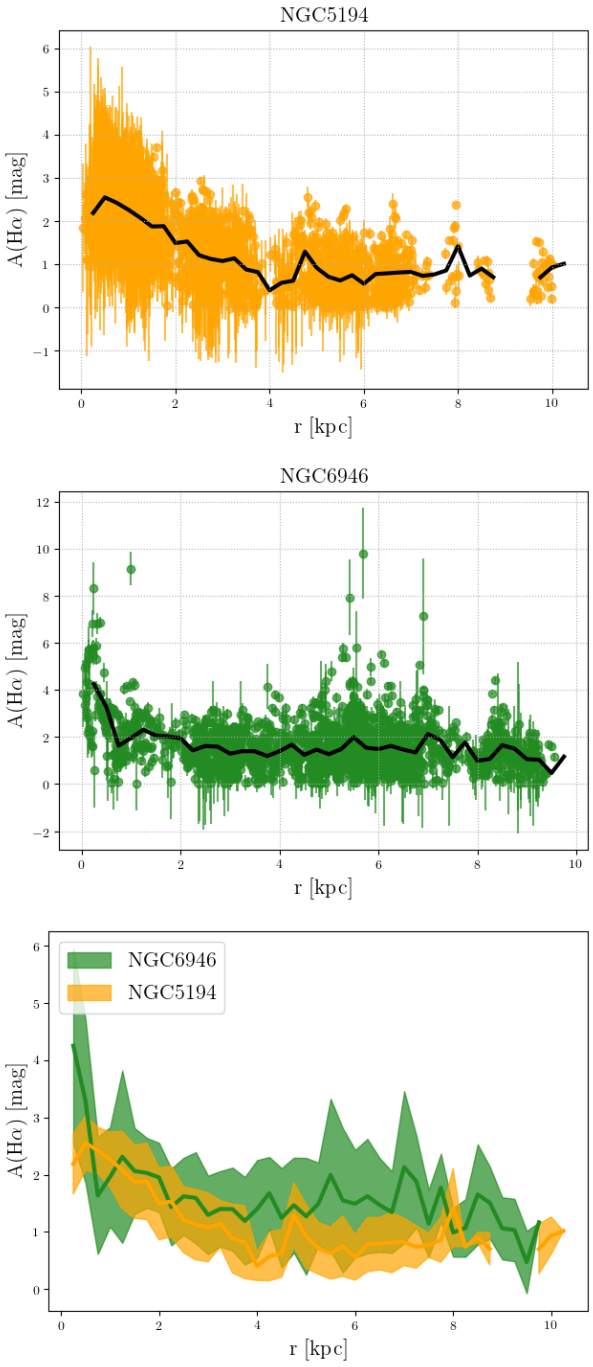

Figure 7. $A(H\alpha)$ **as a function of galactocentric radius.** The lines show median $A(H\alpha)$ in 0.25 kpc-wide bins of galactocentric radius. Points in the top two panels show individual apertures. In the bottom panel the shaded regions show the $\pm 1\sigma$ range in each bin.

Table 6 reports rank correlation coefficients relating the Hα-to-IR color to $A(H\alpha)$ for each band.

Both the Figures and the table show that for all IR bands, the ratio of Hα-to-IR anti-correlates with $A(H\alpha)$. That is, as Hα-to-IR goes up, $A(H\alpha)$ goes down and vice versa. Typical rank correlation coefficients lie in the range -0.45 to -0.6. This is exactly the sense of the Calzetti et al. (2007) and Kennicutt et al. (2007) relations, and this clearly also holds in our data.

As in Calzetti et al. (2007) and Kennicutt et al. (2007), we calibrate linear relations between Hα, IR, and attenuation-corrected $A(H\alpha)$. This linear approach has the advantage of being robust when used across many different spatial scales, at the cost of some potential inaccuracy. We recast this into a model relating $A(H\alpha)$ to the Hα-to-IR ratio:

$$L(\mathrm{H}\alpha)_{\mathrm{corr}} = L(\mathrm{H}\alpha) + \alpha \times (\nu L_\nu(IR)) \quad (6)$$

$$L(\mathrm{H}\alpha)_{\mathrm{corr}} = 10^{A(H\alpha)/2.5} \times L(\mathrm{H}\alpha) \quad (7)$$

$$A(H\alpha) = 2.5 \log_{10}\left(1 + \alpha \times \frac{\nu L_\nu(IR)}{L_{\mathrm{H}\alpha}}\right) \quad (8)$$

where $L(\mathrm{H}\alpha)_{\mathrm{corr}}$ is the attenuation-corrected Hα luminosity in a region, $L(\mathrm{H}\alpha)$ is the measured (i.e., not attenuation-corrected) luminosity in a region, α is an empirical scaling coefficient, and νL_ν is the infrared luminosity of a region. In our cross-scale approach $A(H\alpha)$ is measured at high resolution and $\nu L_\nu / L(\mathrm{H}\alpha)$ is measured at low, matched resolution.

For each IR band, we calculate the correlation coefficients and the empirical scaling factor, α, to translate the Hα-to-IR ratio into an estimate of attenuation. We report these for each galaxy and for both galaxies combined in Table 6. In Table 5, we also give the scatter in $A(H\alpha)$ about the predictions from each prescription for $A(H\alpha)$. Wherever a literature Hα-to-IR ratio is available we plot the expected relation. These are tabulated in Table 6.

In both galaxies the Hα-to-70μm ratio predicts $A(H\alpha)$ with the least amount of scatter. It also boasts the highest correlation coefficient in NGC 5194 and the second highest in NGC 6946. As shown in Table 5, the Hα-to-70μm not only produces the least amount of scatter in $A(H\alpha)$ among the IR models, but produces the least amount of scatter in $A(H\alpha)$ overall. For galaxies like NGC 5194 and NGC 6946, we find the Hα-to-70μm ratio best to predict $A(H\alpha)$.

Central regions: When we calculate the factor α, we omit the central kiloparsec in NGC 6946 and the central 2 kiloparsecs in NGC 5194. This ensures that we are not biased by the AGN in NGC 5194 and ensures that we only use apertures where we are confident in the background subtraction.

Figure 8 shows that this choice to exclude the centers does matter. While a single linear coefficient has trouble predicting $A(H\alpha)$ for all points, our measurements at larger radii, which lie mostly in the spiral arms, agree reasonably with previous results.

This deviation of the center from the overall relationship may reflect a different infrared SED and dust geometry in the galaxy center compared to the disk. In

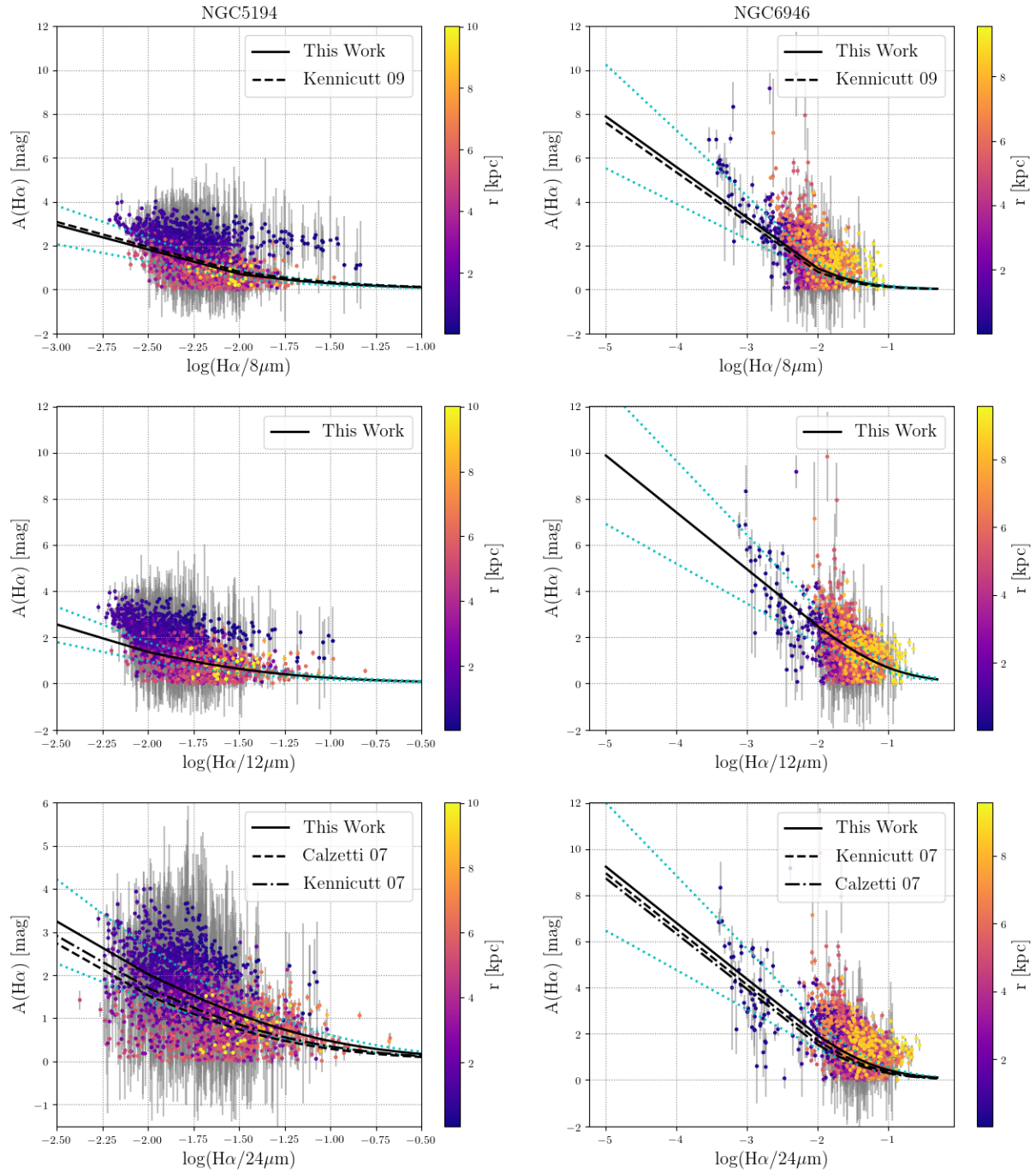

Figure 8. $A(H\alpha)$ **as a function of** Hα**-to-IR color for mid-infrared bands.** Each panel show $A(H\alpha)$ as a function of the ratio between Hα emission and IR emission at one band, either 8, 12, or 24μm. The curves show linear models of the form given in Equation 6. We plot our best fit α (see Table 6) as a solid black curve, with cyan lines indicating $\pm$30% uncertainties on our derived α values. When available, we show literature prescriptions as dashed curves. Note that we derive α excluding the central 2 kpc in NGC 5194 and the center 1 kpc in NGC 6946, which explains some of the low radius deviation from the best-fit trends.

NGC 5194, it might also partially reflect the influence of the AGN. Alternatively, this may reflect the difficulties in establishing a good zero-point for the bright, extended central regions, as discussed above.

In NGC 6946, the very center of the galaxy clearly behaves separately from the rest of the galaxy. Points that have very high values of $A(H\alpha)$ also have very low values of Hα-to-IR. As these points are very bright in the IR,

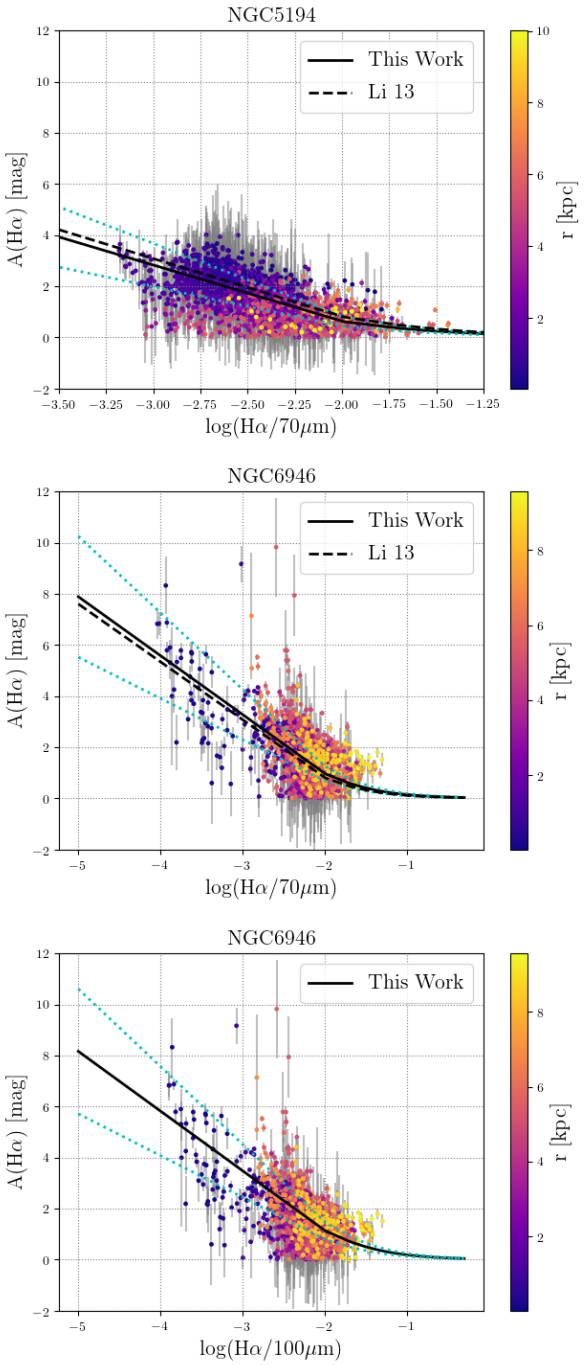

Figure 9. $A(H\alpha)$ **as a function of** Hα**-to-IR color for far-infrared bands.** Similar to Figure 8, each panel shows $A(H\alpha)$ as a function of the ratio between Hα emission and far infrared emission, either at at 70 or (for NGC 6946) 100μm. The curves show linear models of the form in Equation 6. We show both our best fit α (solid black curves) and literature prescriptions (dashed curves). These are summarized in Table 6. Cyan lines indicate ±30% uncertainties on our derived α values. Our fit to α excludes the central 2 kpc in NGC 5194 and the center 1 kpc in NGC 6946. The apertures are color coded by radius in kpc.

this indicates that the high values of $A(H\alpha)$ calculated have merit. Additionally the high values of $A(H\alpha)$ fall along the predicted trends from previous literature measurements. However, the apertures that show very high attenuation values at larger radii from the galaxy center seem to be simple Poisson differences between the Hα map and our Paβ map as points do not seem as bright in the IR as we would expect.

4.2.2. $A(H\alpha)$ *from* Hα *luminosity of each region*

In Figure 10, we compare the calculated value of $A(H\alpha)$ to the Hα luminosity. We plot both the observed luminosity and the attenuation-corrected value.

Comparing $A(H\alpha)$ to the observed Hα luminosity tests whether regions that appear bright before any attenuation correction tend to have high $A(H\alpha)$. We find no significant correlation between L(Hα) and $A(H\alpha)$. The correlation coefficient between the two is -0.06 for NGC 5194 and -0.21 for NGC 6946. Apertures with large values of $A(H\alpha)$ do not appear preferentially bright or dim.

The situation appears dramatically different when we compare $A(H\alpha)$ to the attenuation-corrected Hα luminosity. Here we find a strong correlation. NGC 5194 shows a rank correlation coefficient of 0.71 between $A(H\alpha)$ and attenuation-corrected Hα luminosity, and NGC 6946 shows a rank correlation coefficient of 0.68. The p-values for both are effectively zero. Some of this correlation will be a artifact. $A(H\alpha)$ affects both axes, so that noise in $A(H\alpha)$ induces a positive correlation. But we also saw in the previous section that $A(H\alpha)$ appears higher in IR-bright regions and the inner galaxy. These are systematic trends, not the result of noise, and they have the same sense as what we observe here. More heavily embedded regions, which will also tend to be more IR-bright and lie at lower galactocentric radius, appear more heavily extinguished. And as Figure 10 shows, they also show higher total attenuation-corrected luminosity.

Summarizing, Figure 10 shows that the most intrinsically luminous apertures do appear to show the highest attenuation. This also appears consistent with the previous two section. Put another way, more intrinsically bright HII region are more likely to be heavily affected by dust. However, this conclusion only applies to the attenuation-corrected Hα luminosity (bottom panels). The *observed* Hα luminosity (top panels) does not show a similar trend, due to the effects of attenuation. Therefore we do not recommend using observed Hα luminosity to predict $A(H\alpha)$.

4.2.3. $A(H\alpha)$*from galactocentric radius*

Figure 7 shows that $A(H\alpha)$ does correlate with galactocentric radius. In both galaxies, we find higher $A(H\alpha)$ near the galaxy center and lower values at large radii. But the bottom panel of Figure 7 also shows that the radial distribution of $A(H\alpha)$ differs between NGC 5194

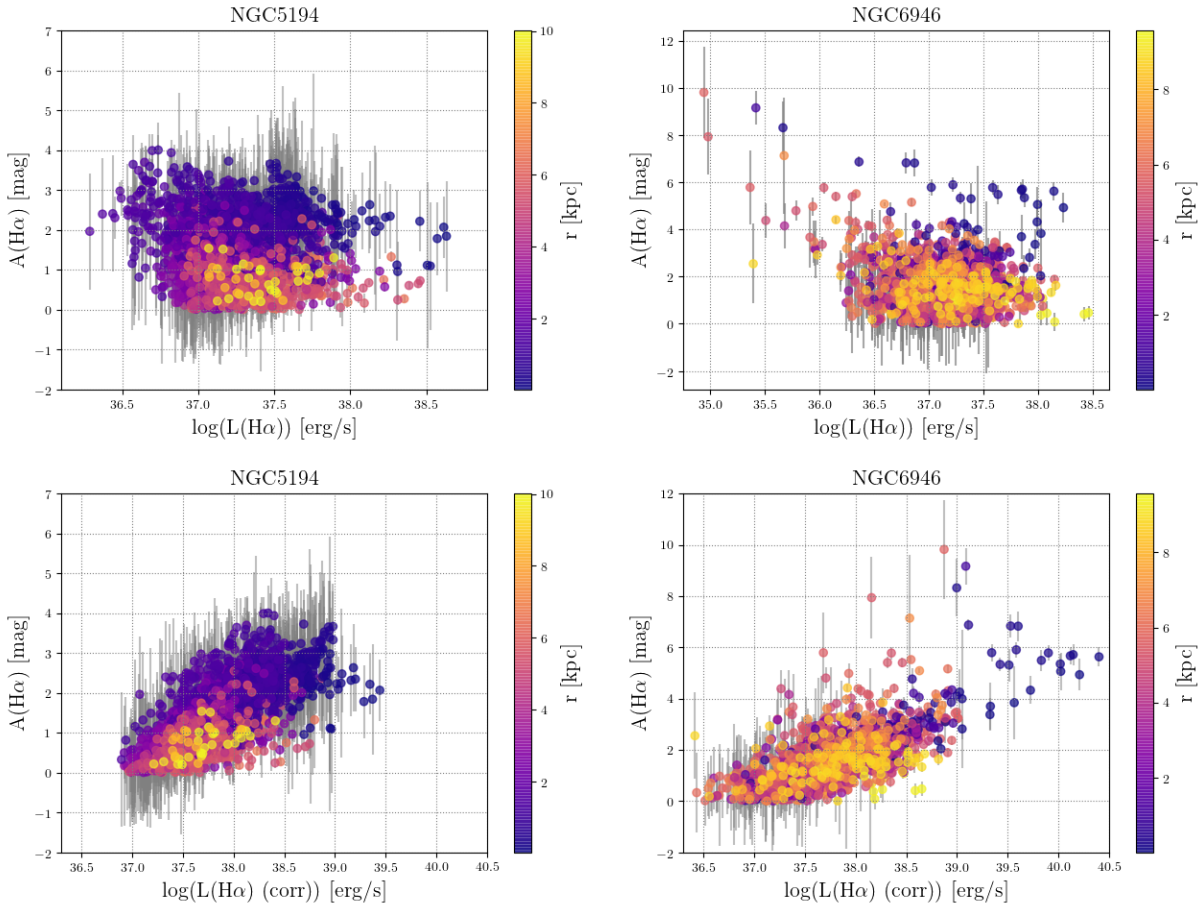

Figure 10. Comparison of $A(H\alpha)$ to Hα luminosity. In the top panels we compare the attenuation in Hα to the luminosity in the same aperture *before* we correct for attenuation. NGC 5194 is on the left and NGC 6946 is on the right. We find no obvious correlation between the two. In the bottom panels, we compare the attenuation in Hα to the luminosity in the same aperture *after* correcting for attenuation. There is a strong positive correlation between $A(H\alpha)$ and attenuation-corrected luminosity.

and NGC 6946. Simply knowing the galactocentric radius, without know what galaxy one is looking at does not offer a good general predictor of $A(H\alpha)$.

To quantify this, we fit an exponential profile to $A(H\alpha)$ as a function of radius in each galaxy. While the exponential can predict the attenuation in $A(H\alpha)$ well for each galaxy individually, the values of the parameters in the fits vary significantly from NGC 6946 ($b = 1.876$) to NGC 5194 ($b = 0.491$), to both galaxies together ($b = 0.991$).

If we had a larger sample size we might be able to fit a general profile, e.g., in which the amplitude and scale length of the $A(H\alpha)$ profile depended on galaxy properties. With a sample size of two, we are not in a position to do more than comment that the profiles appear different. $A(H\alpha)$ drops with radius in both cases, but the profile has different scale lengths and amplitudes in the two galaxies.

4.2.4. $A(H\alpha)$*from gas column density*

The dust that causes attenuation will be mixed with gas, which is mostly either atomic, HI, or molecular, H_2. Thus, the column density of gas should be related to the observed attenuation, modulo uncertainties regarding the geometry and dust-to-gas ratio. The HI gas column can be traced by 21-cm line emission, while the H_2 gas column can be traced by CO line emission.

In Figures 11 and 12 we plot $A(H\alpha)$ as a function of neutral gas column density. In all three Figures, the x-axis shows the total column density of neutral hydrogen, N(H), calculated via:

$$N(H) = N(\mathrm{HI}) + 2 \cdot N(H_2)\ . \tag{9}$$

We calculated $N(\mathrm{HI})$ from 21-cm line maps and $N(H_2)$ from CO line maps as described in Section 2.7. In the top panels of Figures 11 both the CO and HI data have been convolved to a matched $13.3''$ $\sim$ 500 pc resolution. In the bottom panels, we use higher resolution CO data combined with the native (but still low) resolution HI. These CO data have resolution $\sim$ 90 pc for NGC 5194 and $\sim$ 200 pc for NGC 6946. In both cases

we assume that the HI, which has coarser resolution, forms a smooth background. In comparing a low resolution mean column density to a more local $A(H\alpha)$, this exercise resembles what we did for the IR-to-Hα color.

We tabulate the correlation coefficients between $A(H\alpha)$ and gas column density in Table 4.2.4. In Figure 11 we plot $A(H\alpha)$ as a function of $N(H)$ for both galaxies. The top four panels show results at $13''.3 \sim 500$ pc resolution. The bottom panels show results at the highest available resolution. Color coding in the panels reflects both galactocentric radius and the molecular-to-atomic gas ratio.

In each case, we observe a significant correlation, such that we find higher $A(H\alpha)$ at higher $N(H)$. The rank correlation coefficients lie in the range 0.4-0.7, comparable to what we find for the IR-to-Hα ratio. That is, $A(H\alpha)$ correlates with the local gas column density about as well as it correlates with the IR-to-Hα color. For NGC 6946 the correlation improves somewhat, from 0.42 to 0.47, if we use the high resolution CO instead of the $13.3''$ data. The Figure shows that this partially reflects that with higher resolution, the bright, high column central region forms a more continuous distribution with the disk.

Figure 11 also shows that, as expected, gas columns are higher at low radii and that the ISM is mostly molecular in most of our apertures. The molecular fraction correlates with the total column density such the the high-column and low-radius points tend to be overwhelmingly molecular.

The center of NGC 6946 stands out in these plots, with high column density compared to its $A(H\alpha)$. This likely at least partially reflects variations in the CO-to-H_2 conversion factor. We adopted a fixed CO-to-H_2 conversion factor, but Rémy-Ruyer et al. (2014a) have shown that α_{CO} shows a strong radial gradient in this galaxy, with much lower values near the galaxy center. Applying such a variable conversion factor will move the central points to lower column density without affecting their $A(H\alpha)$, bringing the center into better agreement with the rest of the galaxy.

We compare the galaxies to each other in Figure 12. The two galaxies roughly similar trends, with higher values of $A(H\alpha)$ indicating higher values of gas column density. In detail, NGC 5194 shows a better-behaved relation whereas NGC 6946 shows more scatter in both column density and attenuation.

Comparison to simple models: Quantitatively, the relationship between $A(H\alpha)$ and $N(H)$ will reflect the dust-to-gas ratio and the relative placement of dust, Hα emission, and the observer. To explore this, we compare our observations to two simple geometric models, a foreground screen of dust and a smooth mixture of Hα emission and dust.

In both models, we allow the overall normalization of the model to vary. For a Milky Way dust-to-gas ratio, all of the gas column in a foreground screen, and a Cardelli et al. (1989) extinction curve, we expect

$$A(H\alpha)^{\rm MW} \sim 0.86 \cdot \frac{N_H}{1.9 \times 10^{21} {\rm cm}^{-2}} \ {\rm mag} \ . \qquad (10)$$

Deviations from this normalization could reflect that some of the gas is behind the emitting source or that the gas and Hα emission have different distributions on small scales. Most simply, we might expect 50% of the gas to lie behind the emission in a case where Hα comes from a thin layer at the midplane.

We calculate the best-fit screen and mixture models. Here, a "mixture model" means that instead of all light passing through a uniform screen of dust with some fixed value of A(Hα), we consider the Hα emission and attenuation to be evenly mixed. Thus, some of the Hα emission experiences only low $A(H\alpha)$, while other Hα emission experiences attenuation corresponding to the full column density of dust. We implement this model numerically, evenly distributing the Hα emission across $A(H\alpha)$ up to the maximum value of $A(H\alpha)$.

For the screen models, we scale Equation 10 by a factor γ so that:

$$\gamma \equiv \frac{A(H\alpha)}{A(H\alpha)^{\rm MW}} \qquad (11)$$

with $A(H\alpha)^{\rm MW}$ from Equation 10. In the mixture models, we perform an analogous calculation, scaling the total column through the screen by γ.

Figure 11 shows the curves for a full screen of Milky Way-style gas, the best-fit fractional screen (i.e., the full Milky Way screen scaled by the best-fit γ), and the best-fit mixture model. In both galaxies, the full screen model overpredicts the amount of attenuation. Instead, the best-fit screens have $\gamma = 0.206$ in NGC 5194, $\gamma = 0.169$ in NGC 6946, and $\gamma = 0.19$ combining both galaxies. This fractional screen model works particularly well in NGC 5194. In NGC 6946, the fractional screen can describe the data at large radius well, but fails to simultaneously capture the galactic center.

Table 7. Comparing $N(H)$ and $A(H\alpha)$.

Quantity	NGC 5194	NGC 6946
r for $N(H)$ at 500 pc[a]	0.67	0.42
r for $N(H)$ at 90 pc	0.60	–
r for $N(H)$ at 200 pc	–	0.47
Screen γ[b]	0.206	0.169
Screen γ — both galaxies	0.190	

[a] Rank correlation coefficient relating $A(H\alpha)$ to total $N(H) = N({\rm HI}) + 2 \cdot N(H_2)$.

[b] Best-fit conversion from column to $A(H\alpha)$ relative to the expectation for a foreground screen with Milky Way composition (Equations 10 and 11).

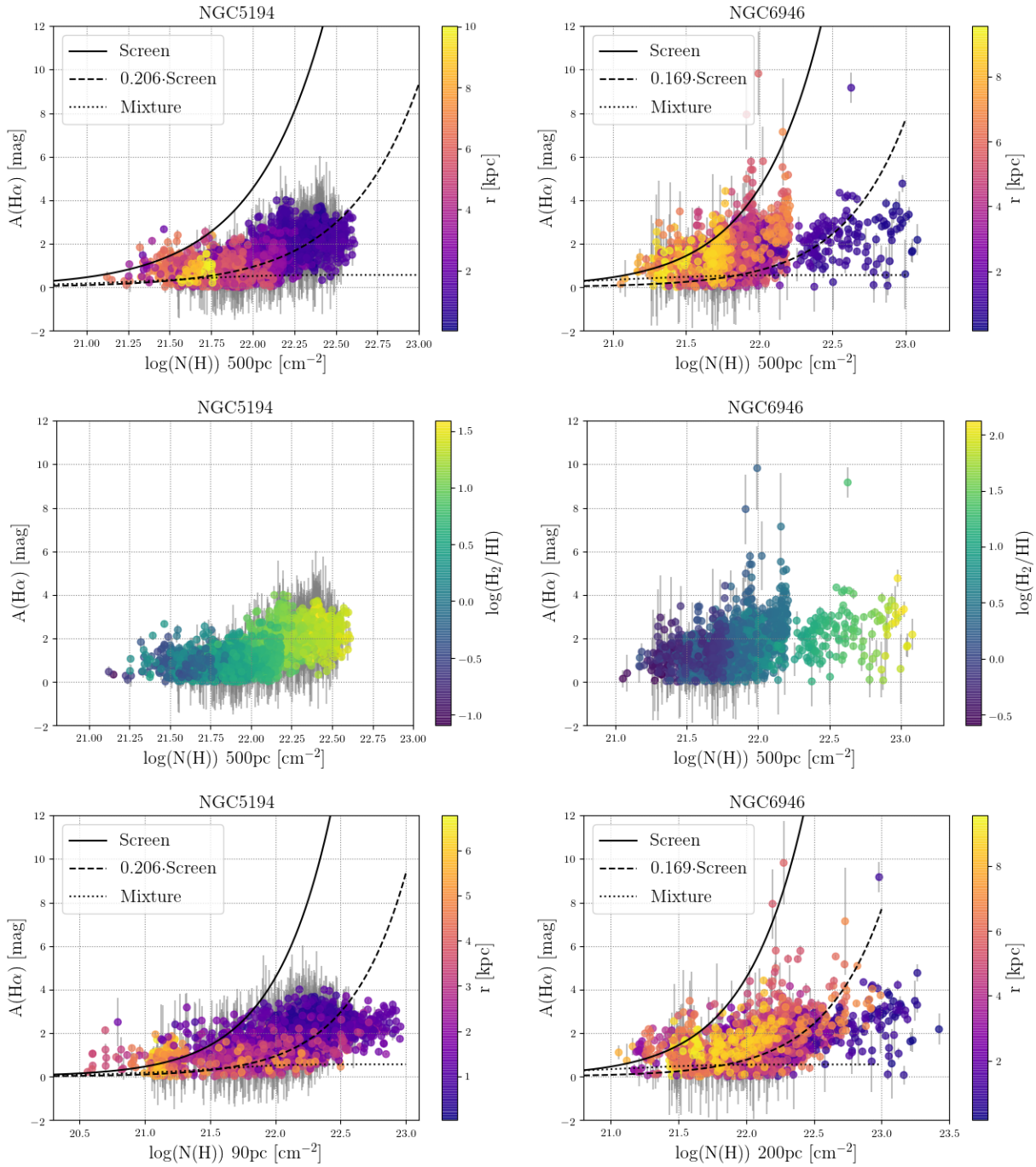

Figure 11. $A(H\alpha)$ **as a function of total (HI+H_2) column density.** Our calculated $A(H\alpha)$ as a function of atomic and molecular gas column density estimated from radio emission line maps. Top: Left: NGC 5194 shows a strong correlation between $A(H\alpha)$ and $N(H)$, which matches a screen model reasonably. Right: NGC 6946 also shows a correlation between $A(H\alpha)$ and $N(H)$, but with a bimodal distribution, similar to the behaviour shown in Figure 8. A screen model where a quarter of the gas contributes to attenuation fits most of the NGC 6946 data well and fits the NGC 5194 data very well. For comparison, we also plot a mixture model (dashed gray line) in which Hα and gas are evenly mixed. In the top and bottom rows, point are color coded by galactocentric radius. In the middle row, points are color coded by the ratio of H_2 to HI column in the aperture. In both galaxies, low $A(H\alpha)$ maps to low column, high radius, and low H_2/HI. The bottom row uses the highest resolution molecular gas map available ($\sim$ 90 pc in NGC 5194 and $\sim$ 200 pc in 6946). The higher resolution map leads to a more continuous behavior at low radii in NGC 6946, though CO-to-H_2 conversion fact effects may also explain the anomalous behavior of the central kpc.

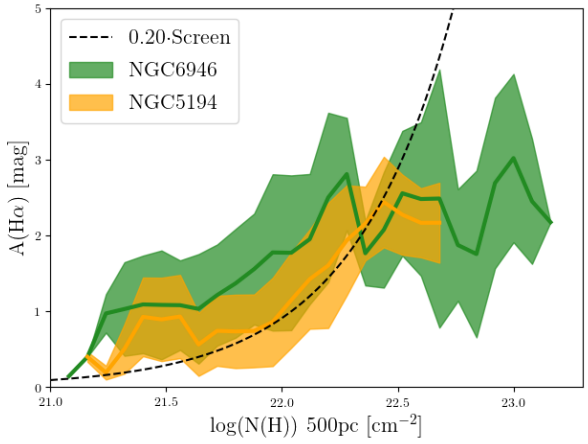

Figure 12. $A(H\alpha)$ **vs.** $N(H)$ **for both galaxies.** Binned trend in $A(H\alpha)$ as a function of total H column at 500 pc resolution for both galaxies. Lines show the median $A(H\alpha)$ at fixed $N(H)$ and the shaded region shows the $\pm 1\sigma$ scatter region. The two galaxies agree relatively well at intermediate $N(H)$. Both appear roughly consistent with a foreground screen with magnitude $\gamma = 0.2$.

We find $\gamma \sim 0.2$. We would expect $\gamma \sim 0.5$ from a smooth screen with half of the gas on the near side of the Hα-emitting region. In principle, lower γ could result from a lower dust-to-gas ratio, but neither NGC 5194 and NGC 6946 are notably low metallicity or dust-poor (e.g., see Aniano et al. 2019). Another, more likely possibility, is that the gas and dust are patchy, with Hα emission and gas imperfectly aligned at small scales. Observations comparing Hα and CO emission at $\sim 1{-}3''$ resolution, including in NGC 5194, appear to show exactly this. Schinnerer et al. (2017) observed offsets between star formation tracers along a spiral arm in NGC 5194. In a systematic analysis of eight spiral galaxies including NGC 5194, Schinnerer et al. (2019) show directly only $\sim 50\%$ of bright Hα and CO are coincident at 140 pc resolution. This is very similar to the scales on which we conduct our analysis and these two results appear consistent.

In this case $\gamma \sim 0.2$ could reflect that half of the dust lies behind the emission, implying $\gamma \sim 0.5$, and that only $\sim 40\%$ of the dust in front of the Hα actually spatially overlaps the Hα. Only this overlapping gas will lead to attenuation, so the effective $\gamma \sim 0.5 \times 0.4 = 0.2$. This patchy scenario would still be consistent with the agreement between the Balmer decrement, Paβ, and 33 GHz emission. It only implies that some of the gas is not actively involved in producing attenuation. We do caution that the resolution mismatch between the gas and the $A(H\alpha)$ estimate renders these numbers even more approximate.

After we fit one free parameter, the gas performs about as well as the IR emission in predicting $A(H\alpha)$. This could be expected, since rank correlation coefficient relating $A(H\alpha)$ to $N(H)$ resembles that seen between $A(H\alpha)$ and IR-to-Hα.

This does not necessarily make gas an equally good predictor of $A(H\alpha)$ compared to IR emission. Some IR bands can be used to predict $A(H\alpha)$ in a way that is robust to metallicity effects and remarkably stable across systems (e.g., see Calzetti et al. 2007, 2010). On the other hand, the gas-to-dust ratio has been shown to depend on metallicity (Draine et al. 2007; Rémy-Ruyer et al. 2014b; Aniano et al. 2019) and the geometry for the gas remains a major uncertainty. We do not necessarily expect $\gamma = 0.2$ to hold generally in the same way as some of the IR-based α values. Still, these kind of gas-attenuation comparisons offer the prospect to learn more about the relative geometry of Hα and dust and could be calibrated into a general tool in future work.

5. SUMMARY AND CONCLUSIONS

We utilized new HST WFC3 Paβ observations of NGC 6946 and archival HST Paβ observations of NGC 5194 to create galaxy-wide Paβ maps. We compared these with archival Hα images to estimate the attenuation affecting the Hα line, $A(H\alpha)$.

We estimate $A(H\alpha)$ in $2''$ diameter apertures placed to cover all regions where Hα emission appears bright enough that we expect to detect Paβ. These apertures cover $\sim 50\%$ of the overall Hα flux from each galaxy. Because the WFC3 mosaics have wide areal coverage, we are able to place many apertures spanning a large range of galactocentric radius in both galaxies. In total, we measure fluxes and line ratios for 2,075 apertures in NGC 5194 and 1,934 apertures in NGC 6946. We tabulate these measurements, the calculated $A(H\alpha)$, and several other quantities of interest in Tables 3 and 2. In NGC 5194 we compare our measurements to recent work using 33 GHz radio data to trace free-free-emission (Querejeta et al. 2019), finding overall consistency between the two data sets.

Treating all apertures equally, NGC 5194 has median $A(H\alpha)$ of 1.4 mag with a 16-84$^{\rm th}$ percentile range of 0.6-2.4 mag. NGC 6946 has median $A(H\alpha)$ of 1.5 mag with 16-84$^{\rm th}$ percentile range 0.7-2.5. The luminosity-weighted mean $A(H\alpha)$ is higher in both galaxies, $\sim$ 2.2 mag in NGC 5194 and ~ 3.4 mag in NGC 6946. In both cases, this reflects heavy attenuation in the inner regions of the galaxy.

In general, we find that the most intrinsically luminous regions show the highest $A(H\alpha)$. However this high attenuation diminishes the apparent Hα luminosity of these regions, so that observed Hα luminosity on its own is not a good predictor of $A(H\alpha)$. Instead, galactocentric radius, the IR-to-Hα ratio, and the local gas column density can all be used to predict $A(H\alpha)$ with varying degrees of accuracy.

We compare $A(H\alpha)$ to the local IR-to-Hα ratio, using IR emission measured at 8, 12, 24, 70, and (for NGC 6946) 100μm. Due to limitations in the data, we

compare our 2″ resolution $A(H\alpha)$ estimates to the IR-to-Hα ratio measured at lower resolution. This resembles the real practical case where IR emission is only available at low resolution and one might wish to estimate the higher resolution, e.g., seeing limited, $A(H\alpha)$. We find a strong anti-correlation between the $A(H\alpha)$ and the IR-to-Hα, in good agreement with Calzetti et al. (2007), Kennicutt et al. (2007), and much following work. For each band, each galaxy, and both galaxies together, we derive best-fit coefficients, α, for linear combinations of Hα and IR. For 12μm, 70μm, and 100μm, these are one of only a few such estimates in the literature. For 8μm, 24μm, and 70μm, our results agree well with previous work, using a large set of individual regions. We also calculate the scatter around each model and tabulate those results in table 5.

Total HI+H_2 gas column density correlates well with $A(H\alpha)$. $N(H)$ shows just as strong of a relationship with $A(H\alpha)$ as IR-to-Hα color in these two galaxies. We compare our measurements to simple models relating gas column to $A(H\alpha)$. Excluding galaxy centers, a screen with $\gamma = 0.2$ times the total expected Milky Way attenuation describes data outside the galaxy centers reasonably well. This could be explained by $\sim 50\%$ of the dust lying behind the emitting regions and a $\sim 40\%$ spatial overlap between gas and Hα emitting regions. Such a low overlap is consistent with recent results showing that Hα and CO resolve into discrete distributions when observed at high physical resolution ($\sim$ 100 pc). Direct, high resolution comparison of $A(H\alpha)$ to gas maps, e.g., with ALMA and JWST, should help further explore this issue.

We thank the anonymous referee for a timely and constructive report that improved this work. We than Knox Long and Rick Pogge for sharing Hα images of NGC 6946 and the HST helpdesk for helpful communications during the processing of the data. The work of SK, was supported by a grant from Program number HST-GO-14156. Support for Program number HST-GO-14156 was provided by NASA through a grant from the Space Telescope Science Institute, which is operated by the Association of Universities for Research in Astronomy, Incorporated, under NASA contract NAS 5-26555. This work was based on observations made with the NASA/ESA Hubble Space Telescope, obtained from the data archive at the Space Telescope Science Institute. STScI is operated by the Association of Universities for Research in Astronomy, Inc. under NASA contract NAS 5-26555. This paper almost makes use of project VLA/14A-171. The National Radio Astronomy Observatory is a facility of the National Science Foundation operated under cooperative agreement by Associated Universities, Inc. The work of SK and AKL is also partially supported by NASA ADAP grants NNX16AF48G and NNX17AF39G and the National Science Foundation grants No. 1615105, 1615109, and 1653300. This research made use of Montage. It is funded by the National Science Foundation under Grant Number ACI-1440620, and was previously funded by the National Aeronautics and Space Administration's Earth Science Technology Office, Computation Technologies Project, under Cooperative Agreement Number NCC5-626 between NASA and the California Institute of Technology.

APPENDIX

A. DETAILS OF THE HST DATA PROCESSING

This appendix details our processing of the HST data. To produce our final Paβ line images, we processed the data using the HST pipeline, used 2MASS to calibrate the zero point of the images, checked the astrometric alignment of the images, estimated and subtracted the stellar continuum, masked foreground stars, and then mosaicked the individual panels into a single image for each galaxy. Much of this processing treated individual images ("panels"). We tabulate the central R.A. and Dec. of each panel in Table 13.

A.1. *Correcting for non-linear backgrounds in the NGC 6946 data*

For NGC 5194 we used standard MAST pipeline products. For NGC 6946, we inspected the FITS images produced by the pipeline. Many images in both filters showed large gradients across the chip. Correspondence with the WFC3 team at STScI revealed this to be caused by a time variable background (TVB).

To correct for this, we re-ran the HST image alignment (`tweakreg`) and drizzling (`astrodrizzle`) pipeline with the original calibrated exposures, or "flt" images. In the ON filter, each calibrated exposure was inspected for TVB effects. Those that did show TVB issues were not included in the subsequent `tweakreg` and `astrodrizzle` pipelines. For the four fields, this led us to use only three of the four observed and calibrated exposures (panels 1, 3, 5, and 7 of the ON data). All of the OFF calibrated exposures were used because there were only two calibrated exposures per field.

Once the TVB calibrated exposures were excluded, we used `tweakreg` to align the calibrated exposures before running the `astrodrizzle` pipeline. We found that the default sky subtraction method ('localmin') produced an all negative background. After trying each sky-subtraction method ('localmin', 'match', 'globalmin', and 'globalmin + match') we found the 'match' sky-subtraction method to yield the best result. This method, which computes differences in sky values between images in common sky regions and "equalizes" sky values, was the only method that produced images absent of all negative backgrounds. We reran the `astrodrizzle` pipeline with these parameters.

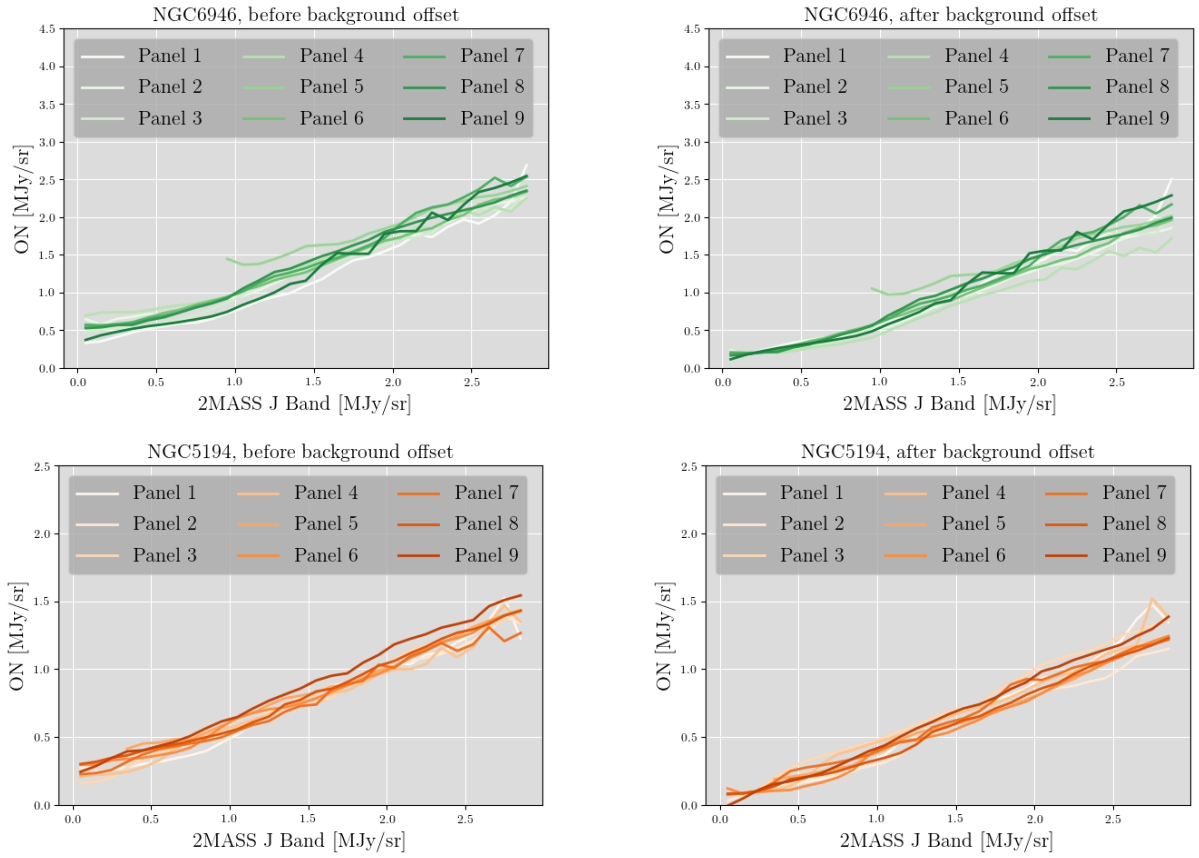

Figure 13. Intensity of HST ON images as a function of 2MASS J band intensity before (top) and after (bottom) matching backgrounds. We anchor the zero point of our HST ON band data to the wide field 2MASS J band images. After matching the resolution and astrometry of the data, we measure the average HST narrow band (ON, F128N) intensity in bins of 2MASS J band intensity. We calculate the offset needed to match the background of the HST images to that of 2MASS and subtract this from the ON images. The bottom row shows the result after this background matching.

The resulting images were mostly free of noticeable TVB issues and negative backgrounds. However, visible issues still affected parts of three panels. These showed horizontal gradients which caused one half of the image to be brighter than the other. We excluded the affected parts of the image that from further analysis. These appear as missing regions in the figures in the main text (e.g., Figures 1 and 3).

A.2. *Background matching and background subtraction*

The field of view of HST is small compared to the size of our galaxies. This leads to a lack of empty sky in most frames, rendering the zero point of our images somewhat uncertain. We take two extra steps to establish a correct zero point and to ensure that the zero point of the ON and OFF images agree.

We anchor our background to J band images from the Two Micron All-Sky Survey (2MASS) (Skrutskie et al. 2006) created by Jarrett et al. (2003). These images have wide area and excellent calibration and sky subtraction. The 2MASS J band filter has peak wavelength of 1.235μm and overlaps both our ON and OFF filters. We matched the background in the high S/N ON images to 2MASS and then used the ON to set the background level in the OFF.

First, we convolved our nine ON images with a Gaussian 2D Kernel of FWHM = 2.5″ (the same PSF as the 2MASS images) and converted all images to have units of MJy sr^{-1}. Then, we reprojected our data onto the 2MASS WCS and astrometrically aligned our images with the 2MASS data. Each image was inspected by eye in order to ensure proper alignment.

Next, we measured the mean intensity of the HST ON data in bins of 2MASS intensity. Fig. 13 shows this comparison. The plot shows a good overall match between our HST images and 2MASS for both galaxies. However, in both cases our ON image still has some positive intensity as the 2MASS image goes to zero. Despite small mismatches in the filter, we expect both images to reflect the same galaxy structure and so go to zero together. Therefore, we

Table 8. Panel centers

Panel	1	2	3	4	5	6	7	8	9
NGC 5194									
... R.A.	202.4191	202.4265	202.4367	202.4572	202.4701	202.4784	202.4998	202.5098	202.5181
... Decl.	47.1564	47.1865	47.2193	47.1553	47.1878	47.2217	47.1570	47.1902	47.2210
NGC 6946									
... R.A.	308.7449	308.6855	308.6260	308.6582	308.7178	308.7774	308.8096	308.7499	308.6903
... Decl.	60.1092	60.1275	60.1455	60.1718	60.1356	60.1356	60.1619	60.1799	60.1980

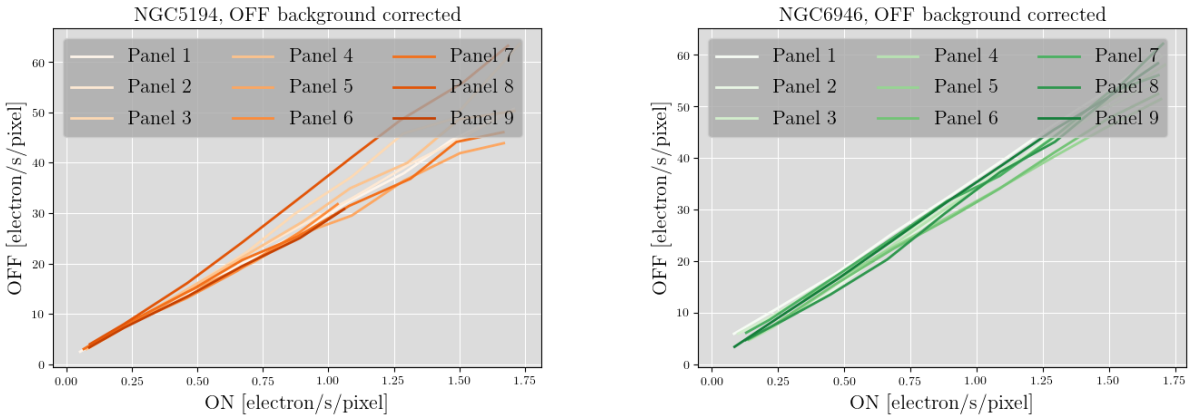

Figure 14. Background matching between the HST ON and OFF images. As Figure 13 but now only showing the OFF intensity as a function of on intensity after matching the zero points between the two images.

calculated the offset needed to bring the ON into agreement with 2MASS for each panel. The average offset was 0.36 MJy sr^{-1} for NGC 6946 and 0.41 MJy sr^{-1} for the NGC 5194. For each panel, we subtracted the calculated offset from the HST ON images in order to match our background to that from 2MASS. The right panels in Figure 13 show the adjusted ON data, which agree well with the 2MASS data.

Next, we match the background in the OFF to the ON. We do this, e.g., rather than independently matching the OFF to 2MASS, because for narrow band imaging purposes, good relative calibration between the line and continuum is essential to a stable result. To match the images, we convolved both the OFF and ON images to 1″. We chose this resolution because it is close to our final working resolution of 2″, and by matching the images at this lower resolution we improve the signal to noise of individual pixels and ensure that any astrometric offsets we encounter (and fix) are relevant to the final analysis at 2″ resolution.

At this stage, we also inspected each image by eye to ensure proper alignment. Then, we matched the OFF to the ON using the same procedure that we used to match the ON to 2MASS. We compare the ON and OFF images after this match in Figure 14, this results in a good match between the ON and OFF data even down to low intensities.

A.3. *Continuum subtraction*

The ON images contain both Paβ and stellar continuum emission. To isolate the Paβ, we use the OFF image to estimate and subtract the contribution of stellar continuum to the ON. Emission in the OFF image represents almost all stellar continuum due to the much wider filter compared to the ON. Because the ON and OFF are so close in wavelength, and because we lack any additional constraints, we adopt a simple model in which the stellar continuum in the ON image is a scaled version of the OFF image. Then:

$$I_{Pa\beta} = I_{ON} - \beta \cdot I_{OFF} \text{ where } \beta = \frac{I_{ON,starlight}}{I_{OFF,starlight}}. \quad \text{(A1)}$$

We derive the scaling factor β empirically, by comparing intensities between the ON and OFF image in regions where we expect both to contain only starlight. To isolate regions with only starlight, we exclude all lines of sight with bright Hα (defined by $I(\text{H}\alpha) > 1\times 10^{-5}$ erg s^{-1} cm^{-2} sr^{-1}) from the analysis. Then, we create an array of possible β

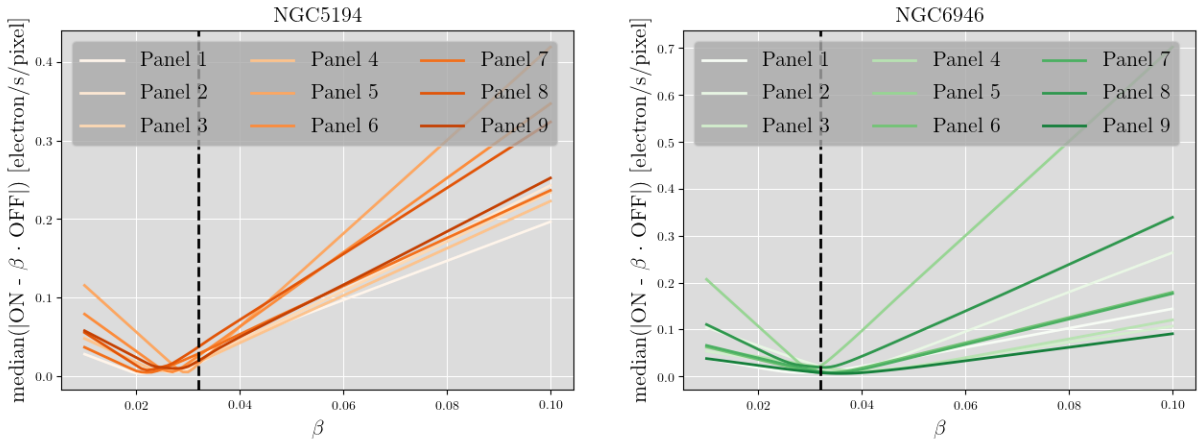

Figure 15. Calibration of the scaling factor used to estimate stellar contamination in the ON using the OFF. The y-axis shows the median absolute difference between the ON and scaled OFF (β·OFF) for possible values of β (x-axis). For each panel, we adopt the β that yields the minimum median absolute value of the difference in regions picked to lack bright Hα. We use this subtract the stellar continuum contribution to the ON image, yielding a final line-only image (Eq. A1). The theoretical scaling factor (0.032) calculated by the ratio of the filter widths is plotted as a vertical black dashed line.

and choose the one that minimizes the median absolute value of the difference between the ON and the scaled OFF. That is, we minimized the median $\mid ON - \beta \cdot OFF \mid$.

We carried out this minimization for each panel. We show the results in Figure 15. We find average $\beta = 0.031$ in NGC 5194, with a 0.001 rms panel-to-panel scatter. We find median $\beta = 0.034$ in NGC 6946, with rms scatter of 0.002. Then, we used the best-fit value of β for each panel to subtract a scaled version of the OFF image to create a Paβ line image. We inspected the final images to verify that our adopted β did not over or under-subtract the continuum.

The Paβ line contributes to the OFF image, but only weakly, $\lesssim 3.6\%$ on average based on our initial estimate of the line maps. This implies that we might slightly over-estimate the stellar continuum in regions where there is bright Paβ. To correct for this, we scale our Paβ image to be 3.6% brighter than our initial estimate.

We use a single, wide-band OFF. Ideally, we would estimate stellar contamination using multiple filters or a narrow band OFF close to ON in wavelength. Our filters lie in the J band near the Rayleigh-Jeans tail of stellar emission, so we do not expect major variations in the color of stellar populations. Modeling of dust attenuation would also benefit from data in multiple bands, but as Paβ emits in the NIR ($\lambda = 1.284\mu$m) we do not expect it to be heavily attenuated by dust. Similarly, we adopt a single β per panel, while in reality we might expect the colors of the stellar population or dust structure to vary across a panel. Finally, we do not have a way to directly account for **any significant** Paβ absorption features in the stellar continuum. We rely on our empirical calibration of the ON-to-OFF ratio to deal with this effect. All of these factors contribute at some level to the overall uncertainty in our final line image.

A.4. *Mosaicking, star masking, and convolution*

After continuum subtraction, we reprojected the individual panels for each galaxy to create a single mosaic image. We used `Montage` to create the mosaic images of both NGC5914 and NGC 6946. We trust our earlier background subtraction and therefore we do not allow `montage` to change the background at this stage.

Both galaxies had foreground and saturated stars in the mosaicked images. As NGC 6946 lies at low Galactic latitude ($b = 11.7°$) it so shows many more foreground stars than NGC 5194. We masked foreground and saturated stars by eye before any subsequent analysis or convolution was done.

After the foreground and saturated stars were masked, the moasicked images for both galaxies were convolved to a Gaussian 2D PSF of $2''$. This matches the working resolution of our Hα maps and ensures that the data used in our analysis have matched PSFs.

A.5. *Correction for Galactic extinction*

We correct both the Paβ and archival Hα for the effects of Galactic extinction. We adopt foreground extinction estimates from Schlafly & Finkbeiner (2011), via the NASA Extragalactic Database. Then we translate these from A_V to $A(H\alpha)$ and $A(Pa\beta)$ using our adopted extinction curve. We scale the whole map for each line by this value. For NGC 5194 our best-estimate Milky Way $A(H\alpha)$ is 0.084 mag and our best-estimate for $A(Pa\beta)$ is 0.026 mag. For NGC 6946 the values are higher. We calculate Milky Way $A(H\alpha)$ of 0.810 mag and $A(Pa\beta)$ of 0.253 mag.

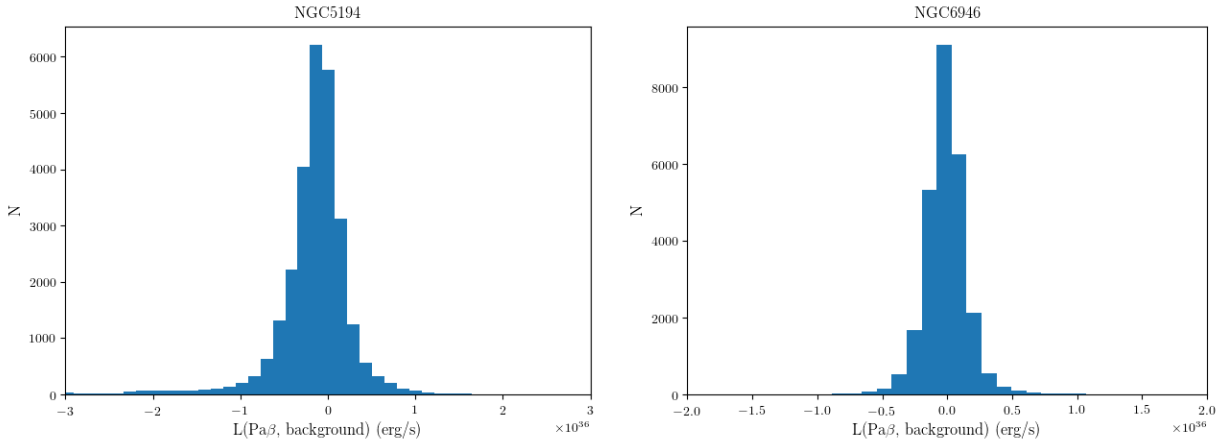

Figure 16. Statistical noise estimates from NGC 5194 and NGC 6946 Paβ maps. Histograms of the luminosities of apertures placed in apparently empty regions of NGC 5194 (left) and NGC 6946 (right).

A.6. *Uncertainties in the final line maps*

We estimate the statistical noise in our final mosaicked images by measuring the standard deviation within an empty patch of sky at 2″ resolution. In NGC 5194 the rms statistical noise is 1.46×10^{-6} erg s^{-1} cm^{-2} sr^{-1}. In NGC 6946, the uncertainty is 5.63×10^{-7} erg s^{-1} cm^{-2} sr^{-1}. In addition to these statistical uncertainties, the broad band filters (our OFF images) of HST's WFC3 have a reported calibration error of ∼2-3% and the narrow band filters (our ON) have a reported photometric error of ∼5-7%. Together, these imply an overall flux calibration uncertainty of $\sim 8-9\%$.

There is also an uncertainty associated with our continuum subtraction. The ON/OFF ratio used for subtraction can reasonably vary by 5×10^{-4}. To quantify this uncertainty we make six maps that vary from visibly over-subtracted to visibly under-subtracted. These maps are then used in our Monte Carlo analysis of our errors in Section 3.5.

REFERENCES

Aniano, G., Draine, B. T., Gordon, K. D., & Sandstrom, K. 2011, Publications of the Astronomical Society of the Pacific, 123, 1218

Aniano, G., Draine, B. T., Hunt, L. K., et al. 2019, arXiv e-prints, arXiv:1912.04914. https://arxiv.org/abs/1912.04914

Beck, S. C., & Beckwith, S. V. 1984, MNRAS, 207, 671, doi: 10.1093/mnras/207.4.671

Bendo, G. J., Galliano, F., & Madden, S. C. 2012, Monthly Notices of the Royal Astronomical Society, 423, 197, doi: 10.1111/j.1365-2966.2012.20784.x

Binder, B. A., & Povich, M. S. 2018, ApJ, 864, 136, doi: 10.3847/1538-4357/aad7b2

Blanc, G. A., Heiderman, A., Gebhardt, K., Evans, N. J., & Adams, J. 2009, The Astrophysical Journal, 704, 842, doi: 10.1088/0004-637x/704/1/842

Bolatto, A. D., Wolfire, M., & Leroy, A. K. 2013, ARA&A, 51, 207, doi: 10.1146/annurev-astro-082812-140944

Calzetti, D. 2013, Star Formation Rate Indicators, ed. J. Falcón-Barroso & J. H. Knapen, 419

Calzetti, D., Kennicutt, Jr., R. C., Bianchi, L., et al. 2005, ApJ, 633, 871, doi: 10.1086/466518

Calzetti, D., Kennicutt, R. C., Engelbracht, C. W., et al. 2007, ApJ, 666, 870, doi: 10.1086/520082

Calzetti, D., Wu, S., Hong, S., et al. 2010, ApJ, 714, 1256, doi: 10.1088/0004-637X/714/2/1256

Cardelli, J. A., Clayton, G. C., & Mathis, J. S. 1989, ApJ, 345, 245, doi: 10.1086/167900

Catalán-Torrecilla, C., Gil de Paz, A., Castillo-Morales, A., et al. 2015, A&A, 584, A87, doi: 10.1051/0004-6361/201526023

Collaboration, T. A., Price-Whelan, A. M., Sipcz, B. M., et al. 2018, The Astronomical Journal, 156, 123

Colombo, D., Hughes, A., Schinnerer, E., et al. 2014, ApJ, 784, 3, doi: 10.1088/0004-637X/784/1/3

Condon, J. J. 1992, ARA&A, 30, 575, doi: 10.1146/annurev.aa.30.090192.003043

Croxall, K. V., Pogge, R. W., Berg, D. A., Skillman, E. D., & Moustakas, J. 2015, The Astrophysical Journal, 808, 42, doi: 10.1088/0004-637x/808/1/42

de Blok, W. J. G., Walter, F., Brinks, E., et al. 2008, AJ, 136, 2648, doi: 10.1088/0004-6256/136/6/2648

Donovan Meyer, J., Koda, J., Momose, R., et al. 2012, ApJ, 744, 42, doi: 10.1088/0004-637X/744/1/42

Draine, B. T., Dale, D. A., Bendo, G., et al. 2007, ApJ, 663, 866, doi: 10.1086/518306
Eldridge, J. J., & Xiao, L. 2019, MNRAS, L37, doi: 10.1093/mnrasl/slz030
Engelbracht, C. W., Rieke, M. J., Rieke, G. H., & Latter, W. B. 1996, ApJ, 467, 227, doi: 10.1086/177598
Epinat, B., Amram, P., Marcelin, M., et al. 2008, MNRAS, 388, 500, doi: 10.1111/j.1365-2966.2008.13422.x
Fitzpatrick, E. L. 1999, PASP, 111, 63, doi: 10.1086/316293
Haffner, L. M., Dettmar, R. J., Beckman, J. E., et al. 2009, Reviews of Modern Physics, 81, 969, doi: 10.1103/RevModPhys.81.969
Ho, P. T. P., Beck, S. C., & Turner, J. L. 1990, ApJ, 349, 57, doi: 10.1086/168293
Hummer, D. G., & Storey, P. J. 1987, MNRAS, 224, 801820, doi: https://doi.org/10.1093/mnras/224.3.8010
Jarrett, T. H., Chester, T., Cutri, R., Schneider, S. E., & Huchra, J. P. 2003, AJ, 125, 525, doi: 10.1086/345794
Kennicutt, R. 1998, Annual Review of Astronomy and Astrophysics, 36, 189, doi: 10.1146/annurev.astro.36.1.189
Kennicutt, R. C., & Evans, N. J. 2012, ARA&A, 50, 531, doi: 10.1146/annurev-astro-081811-125610
Kennicutt, R. C., Calzetti, D., Aniano, G., et al. 2011, PASP, 123, 1347, doi: 10.1086/663818
Kennicutt, Jr., R. C., Armus, L., Bendo, G., et al. 2003, PASP, 115, 928
Kennicutt, Jr., R. C., Calzetti, D., Walter, F., et al. 2007, ApJ, 671, 333, doi: 10.1086/522300
Kreckel, K., Groves, B., Schinnerer, E., et al. 2013, ApJ, 771, 62, doi: 10.1088/0004-637X/771/1/62
Kroupa, P. 2001, MNRAS, 322, 231, doi: 10.1046/j.1365-8711.2001.04022.x
Leitherer, C., Schaerer, D., Goldader, J. D., et al. 1999, ApJS, 123, 3, doi: 10.1086/313233
Leroy, A. K., Walter, F., Bigiel, F., et al. 2009, AJ, 137, 4670, doi: 10.1088/0004-6256/137/6/4670
Leroy, A. K., Lee, C., Schruba, A., et al. 2013a, ApJL, 769, L12, doi: 10.1088/2041-8205/769/1/L12
—. 2013b, ApJL, 769, L12, doi: 10.1088/2041-8205/769/1/L12
Leroy, A. K., Sandstrom, K. M., Lang, D., et al. 2019, ApJS, 244, 24, doi: 10.3847/1538-4365/ab3925
Li, Y., Crocker, A. F., Calzetti, D., et al. 2013, ApJ, 768, 180, doi: 10.1088/0004-637X/768/2/180
Long, K. S., Winkler, P. F., & Blair, W. P. 2019, ApJ, 875, 85, doi: 10.3847/1538-4357/ab0d94
Luridiana, V., Morisset, C., & Shaw, R. A. 2015, A&A, 573, A42, doi: 10.1051/0004-6361/201323152
McQuinn, K. B. W., Skillman, E. D., Dolphin, A. E., Berg, D., & Kennicutt, R. 2016, ApJ, 826, 21, doi: 10.3847/0004-637X/826/1/21
Mentuch Cooper, E., Wilson, C. D., Foyle, K., et al. 2012, ApJ, 755, 165, doi: 10.1088/0004-637X/755/2/165
Murphy, E. J., Dong, D., Momjian, E., et al. 2018, ApJS, 234, 24, doi: 10.3847/1538-4365/aa99d7
Murphy, E. J., Condon, J. J., Schinnerer, E., et al. 2011, ArXiv e-prints. https://arxiv.org/abs/1105.4877
Murphy, E. J., Bremseth, J., Mason, B. S., et al. 2012, ApJ, 761, 97, doi: 10.1088/0004-637X/761/2/97
Querejeta, M., Schinnerer, E., Schruba, A., et al. 2019, A&A, 625, A19, doi: 10.1051/0004-6361/201834915
Quillen, A. C., & Yukita, M. 2001, AJ, 121, 2095, doi: 10.1086/319949
Rebolledo, D., Wong, T., Xue, R., et al. 2015, ApJ, 808, 99, doi: 10.1088/0004-637X/808/1/99
Rémy-Ruyer, A., Madden, S. C., Galliano, F., et al. 2014a, A&A, 563, A31, doi: 10.1051/0004-6361/201322803
—. 2014b, A&A, 563, A31, doi: 10.1051/0004-6361/201322803
Schinnerer, E., Böker, T., Emsellem, E., & Lisenfeld, U. 2006, ApJ, 649, 181, doi: 10.1086/506265
Schinnerer, E., Meidt, S. E., Pety, J., et al. 2013, ApJ, 779, 42, doi: 10.1088/0004-637X/779/1/42
Schinnerer, E., Meidt, S. E., Colombo, D., et al. 2017, ApJ, 836, 62, doi: 10.3847/1538-4357/836/1/62
Schinnerer, E., Hughes, A., Leroy, A., et al. 2019, ApJ, 887, 49, doi: 10.3847/1538-4357/ab50c2
Schlafly, E. F., & Finkbeiner, D. P. 2011, ApJ, 737, 103, doi: 10.1088/0004-637X/737/2/103
Schuster, K. F., Kramer, C., Hitschfeld, M., Garcia-Burillo, S., & Mookerjea, B. 2007, A&A, 461, 143, doi: 10.1051/0004-6361:20065579
Scoville, N. Z., Stolovy, S. R., Rieke, M., Christopher, M., & Yusef-Zadeh, F. 2003, The Astrophysical Journal, 594, 294, doi: 10.1086/376790
Skrutskie, M. F., Cutri, R. M., Stiening, R., et al. 2006, AJ, 131, 1163, doi: 10.1086/498708
Smith, J. D. T., Draine, B. T., Dale, D. A., et al. 2007, ApJ, 656, 770, doi: 10.1086/510549
Tomičić, N., Ho, I.-T., Kreckel, K., et al. 2019, ApJ, 873, 3, doi: 10.3847/1538-4357/ab03ce
Tsai, C.-W., Turner, J. L., Beck, S. C., Meier, D. S., & Wright, S. A. 2013, ApJ, 776, 70, doi: 10.1088/0004-637X/776/2/70
Turner, J. L., Ho, P. T. P., & Beck, S. 1987, ApJ, 313, 644, doi: 10.1086/165003
Walter, F., Brinks, E., de Blok, W. J. G., et al. 2008, AJ, 136, 2563, doi: 10.1088/0004-6256/136/6/2563